THE
PHYSICAL REVIEW
A Journal of Experimental and Theoretical Physics Established by E. L. Nichols in 1893
VOL. 60, NO. 5 SEPTEMBER 1, 1941 SECOND SERIES

Scattering of Protons by Magnesium and Aluminum

T. R. WILKINS*
University of Rochester, Rochester, New York
(July 14, 1941)

A new type of nuclear scattering camera utilizing photographic emulsions to determine number and energy of scattered protons at many sharply defined angles is described and compared with earlier experimental arrangements. A survey of the effects of various factors in producing straggling of the scattered particles is presented. The angular distributions of elastically and inelastically scattered proton groups are presented, and the former compared with Rutherford scattering. Excited states of magnesium nuclei are found to occur at 1.37 Mev, 2.80 Mev, and 4.07 Mev.

INTRODUCTION

IT has been recognized that much valuable experimental information concerning the fields of force about atomic nuclei of the lighter elements can be gained by a direct study of the scattering of protons, deuterons and alpha-particles by such nuclei.[1] Yet relatively few experimental results have been published in this field in recent years,[2–15] and the majority of these were obtained only with alpha-particles.

Published results have appeared in two general forms. In one procedure the ratio of observed to expected or classical yield of particles scattered through a selected scattering angle has been measured as a function of the energy of the bombarding particles. Another procedure has included measurement of the same ratio as a function of the angle of scattering for bombarding particles of constant incident energy. The expected or classical yield is that predicted by Rutherford's theory[16] for scattering of particles by an inverse square field of force. Where the scattering of large numbers of particles has been studied, no publications have, until recently,[8,10,11,14] contained measurements of the energy distribution of the scattered particles.

* Because of the untimely death of Professor T. R. Wilkins this work has been completed and presented by Gerald A. Wrenshall, McMaster University, Hamilton, Canada.

[1] H. A. Bethe, Rev. Mod. Phys. **9**, 69 (1937).
[2] E. S. Bieler, Proc. Roy. Soc. **A105**, 434 (1924).
[3] E. Rutherford and Chadwick, Phil. Mag. **50**, 889 (1925).
[4] Reizler, Proc. Roy. Soc. **A134**, 154 (1932).
[5] Reizler, Ann. d. Physik **23**, 198 (1935).
[6] G. Brubaker, Phys. Rev. **54**, 1011 (1938).
[7] S. Devons, Proc. Roy. Soc. **A172**, 127 (1939).
[8] T. R. Wilkins and G. Kuerti, Phys. Rev. **55**, 1134A (1939).
[9] G. Kuerti and T. R. Wilkins, Phys. Rev. **57**, 1081 (1940).
[10] T. R. Wilkins and G. Kuerti, Phys. Rev. **57**, 1083 (1940).
[11] Powell, May, Chadwick, and Pickavance, Nature **145**, 893 (1940).
[12] Kanne, Taschek, and Ragan, Phys. Rev. **58**, 693 (1940).
[13] A. J. Ferguson and L. R. Walker, Phys. Rev. **58**, 666 (1940).
[14] T. R. Wilkins and G. Wrenshall, Phys. Rev. **58**, 758 (1940).
[15] Schultz, Davidson, and Ott, Phys. Rev. **58**, 1043 (1940).
[16] E. Rutherford, Phil. Mag. **21**, 669 (1911).

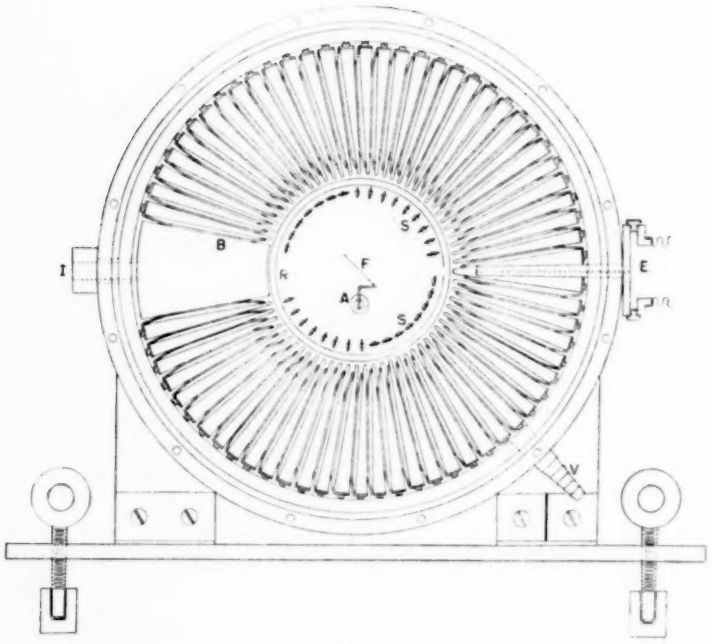

(a)

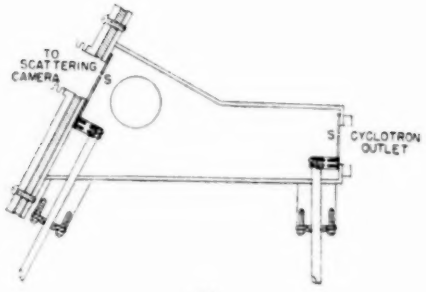

(b)

FIG. 1(a) and (b). The scattering camera and additional collimating slits. Connecting sylphon tube is not shown.

The general lack of intense sources of protons, deuterons and alpha-particles until recent years, and of suitable means of faithfully registering scattered particles for long periods of time, has forced investigators in this field to use poorly defined scattering angles in order to obtain results. This lack of precision has rendered theoretical analyses of experimental results somewhat inconclusive.[17] Both of these deficiencies have been improved upon in the present analysis, in which measurement of the yield of scattered particles at a series of sharply defined angles is attempted. A cyclotron is used to produce a sufficiently intense and homogeneous source of bombarding particles (protons). The yield and energy of scattered protons at the selected scattering angles are measured from the number and length of the discrete tracks produced in suitable photographic emulsions by the passage of these particles.

EXPERIMENTAL

A scattering camera consisting of a flat cylindrical container made of brass 0.9 cm thick, and of about 30 cm outside diameter and 5.0 cm depth has been employed. It contains a series of sixty-six photographic plateholders set fan-wise at five-degree intervals about a central scattering foil F (Fig. 1(a)) so that angular scattering over the range 15° to 170° can be studied. The plateholders are arranged so that particles entering the camera at E and scattered by F enter the emulsion surface of each ($1''\times3''$) photographic plate at a grazing angle of 4°. The ensemble of plateholders is milled from a single disk of brass. Each photographic plate is held firmly in position by a flat bow spring B.

Between scattering foil and photographic plates there is a brass ring R in which are drilled the series of 0.09-cm diameter beveled holes which, with the scattering foil and the apertures through which the incident beam enters, define the angles through which the scattered particles pass to the photographic plates. The particles thus scattered produce flat parallel tracks in the photographic emulsion distributed over a very restricted area (1.0×0.1 cm), so that tracks produced by extraneous particles are easily recognized and eliminated from records.

Shutters S make it possible to block any of the apertures in R during a run if exposures of differing amounts are desired for different angles. Varying exposures are clearly very necessary, especially at smaller scattering angles, if the

[17] P. Seligmann, Phys. Rev. **58**, 492 (1940).

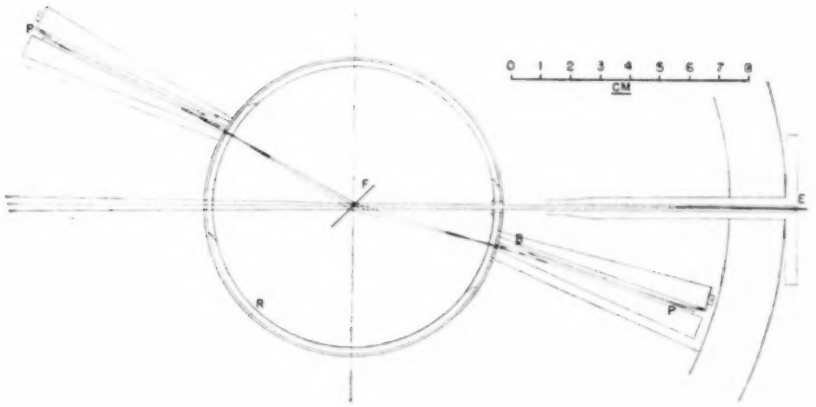

FIG. 2. Degree of angular definition of scattering camera shown at two characteristic angles. Representative photographic plates *P* are shown.

distribution of scattered particles varies in approximate accordance with Rutherford's theory. Each shutter consists of a brass plate fastened to a tapered rotatable brass plug situated in the removable side of the camera, and serves to cover two adjacent apertures in *R*. To measure exposures, a current integrator at *I*, attached to an ionization chamber registers the beam after it has passed through the camera, so that suitable relative exposures of the photographic plates can be measured. A vacuum is maintained throughout the entire camera system by means of a pumping system attached at *V*.

Stopping foils of aluminum inserted between scattering foil and photographic plates reduce the ranges of scattered particles by known amounts to lengths suitable for registration in the plates, and also reduce an effect which is roughly equivalent to additional straggling which shall be referred to as apparent straggling, caused by the inequality in stopping power of the component parts of the photographic emulsion. The stopping foils are located in a rectangular ring trough cut on the inner side of *R*. The scattering foil *F* is placed at 45° to the beam, allowing simultaneous exposure of thirty-three plates distributed over diametrically opposed forward and backward quadrants of the camera. *F* can be rotated out of the beam, and accurately returned to its original position by a tapered brass arm *A* by which it is supported. *A* extends through the back of the camera, and can be adjusted during an experimental run. It may be replaced during a run by a second similar scattering foil arrangement not shown in Fig. 1(a) by which the remaining two quadrants of the camera can be used.

The angular definition of the camera proper is shown in Fig. 2 in terms of the camera's geometry. The individual scattering angles thus defined cannot vary from their mean value by more than about $\pm 1.2°$. However, in addition to this definition, the beam is further restricted as it leaves the cyclotron by two 1.0 mm wide slits *S* (Fig. 1(b)) spaced 16 cm apart, after which it passes through an evacuated sylphon tube for a distance of 122 cm before reaching the camera. If it be assumed that the paths of the particles in this section are rectilinear, their maximum angular spread on scattering to a given photographic plate is reduced to about $\pm 0.5°$. From these considerations it is felt that the maximum angular variation does not exceed $\pm 1°$.

Throughout the present series of experiments, a single lot of Eastman Kodak "fine-grain alpha-particle" photographic plates have been used. The relative stopping power of these plates was obtained primarily by measuring the lengths of alpha-particle tracks of known energy. The emulsion sensitization, processing, and microscope techniques used have been described elsewhere.[18] However, certain refinements have been made. To permit systematic counting of tracks and to have a check on the magnification of the microscope, each plate was marked photographically with a series of straight lines perpendicular to the direction of the emulsion tracks, and spaced 0.25 mm apart. These lines

[18] T. R. Wilkins, J. App. Phys. **11**, 35 (1940).

were prevented from penetrating deeply into the body of the emulsion by making the necessary exposure with ultraviolet light. This permits emulsion tracks located deep in the emulsion to be resolved more readily than if more penetrating illumination were used. The necessity for using depth focusing in emulsion track work is really an advantage in that it usually permits an observer to distinguish between the ever-present "fog" particles in the emulsion and the true ends of particle tracks. However, it makes impractical the publication of a clear photograph of emulsion tracks in this experiment.

Because of the considerable eyestrain and fatigue caused by long periods of close examination with a microscope, the microscopic image of the tracks was projected onto a vertical ground glass screen, with ground side toward the microscope. In contact with this side was mounted a frame carrying a series of twelve fine taut steel wires, spaced 0.8 cm apart, which crossed the track images at right angles and permitted the accurate measurement of emulsion track lengths. A large plano-convex lens mounted on the observer's side of the ground glass screen converges the light so that all parts of a track image can be viewed simultaneously. This arrangement has been found to be much less tiring to operate than the usual binocular or monocular microscope with eyepiece scale. Depth focus and the mechanical stage of the microscope are operated by the left hand, leaving the right hand free to record measurements.

The intense illumination required for dark-field projection was obtained from an automatic feed arc lamp. Best results were obtained by using small diameter cored carbons to prevent wandering of the arc spot, and consequent fluctuations in the brightness of the projected images. The light beam was heat filtered by passage through a water solution of copper chloride.

Accuracy of Observations

(1) Factors affecting width of distribution peaks

It is of some interest to investigate the relative importance of the factors which contribute to the breadth of the distribution peaks obtained by plotting the frequency against length of emulsion tracks, the peaks representing proton groups. The factors will include the normal straggling of the protons in the homogeneous stopping and scattering foils, apparent straggling, and error in measurement of track lengths due to least count and grain spacing along tracks in the photographic emulsion. Superimposed on these will be the effects of inhomogeneity of the proton beam as it arrives at the scattering camera, and, in the case of magnesium, the broadening of the peak produced by elastic scattering due to the inherent presence of the three important isotopes. In Table I are presented measurements made at four representative angles on the widths of the distribution peaks for 6.9-Mev protons scattered by magnesium using the scattering camera. All of the photographic plates were simultaneously exposed, and were analyzed by the same observer using the same microscope.

Examination of the scattering arrangements of the camera as shown in Fig. 2 shows that the mean straggling of a homogeneous beam of bombarding particles, scattered back through the same surface of foil through which they entered, will, to a fair approximation, be greater than for particles scattered through the opposite side by the air equivalent of the scattering foil. This statement refers specifically to the arrangement used and shown in Fig. 1, namely where photographic plates are exposed only in the diametrically opposed quadrants of the camera indicated by the normals to the scattering foil. For a homogeneous proton beam there would thus be a relatively large increase in the straggling of scattered particles for scattering angles greater than 90°, roughly proportional to scattering foil thickness. But when the other factors previously mentioned produce distribution curves of considerable average width, this effect is reduced in importance since it is not additive. For example, in this experiment the

Table I. *Mean peak half-widths, in cm of equivalent air, of distribution curves produced by protons scattered elastically (E), and inelastically (I_1) by magnesium.*

Scattering angle	60°	80°	125°	145°	Average
E peak half-width	2.32	2.35	2.26	2.57	2.38
I_1 peak half-width	1.69	2.04	2.07	2.15	2.00

average increase in straggling for scattering angles greater than 90° would have been ±0.62 cm air for a homogeneous beam of bombarding protons, while actually for the representative results of Table I it produced a mean peak width increase of only $\pm(2.26-2.10)=\pm 0.16$ cm air straggling. Hence it would appear that this factor in broadening the large-angle scattering peaks is relatively ineffective in this experiment due to the presence of more important factors.

Because of the dependence of recoil energy of a scattering nucleus on its mass, a beam of homogeneous protons scattered by a mixture of the Mg isotopes would appear in the elastic scatter peak as three components slightly displaced relative to each other. A simple calculation shows that the displacement of the three isotope peaks would be slight in the present case, being of the order of 0.02 Mev. This would be scarcely detectable keeping in mind that Mg^{24} constitutes 80 percent of normal magnesium. It would at most produce a slight distortion of the elastic scatter peak on the high energy side, an effect which is not observed here.

An indication of the apparent straggling effect which the inhomogeneous photographic emulsion produces can be found by comparing the average widths of the two main scatter peaks in Mg. The elastic scatter peak should be the broader of the two due to the greater path of its particles through the photographic emulsion. This is seen to be true for the representative results in Table I. There is an average increase in the width of the elastic scatter peak over that of the inelastic scatter peak of $\pm(2.38-2.00)=\pm 0.38$ cm air. The corresponding increase in mean peak width for passage of the proton beam through a thickness of air equivalent in stopping power to the emulsion thickness between the peaks considered is ±0.19 cm air. Thus the photographic emulsion inhomogeneity roughly doubles the straggling in our work.[19]

Uncertainties in measuring track lengths due to the finite spacing of silver grains defining the tracks, and by least count error in estimating track lengths, are of the same order of magnitude. The average grain spacing for protons was found to be about 0.1 scale division in track length. Track lengths were measured to the nearest tenth of a scale division. It is estimated that, combined, these effects produce an average uncertainty in track range measurements of ±0.6 cm of equivalent air.

Since protons were allowed to enter the photographic emulsion at a mean grazing angle

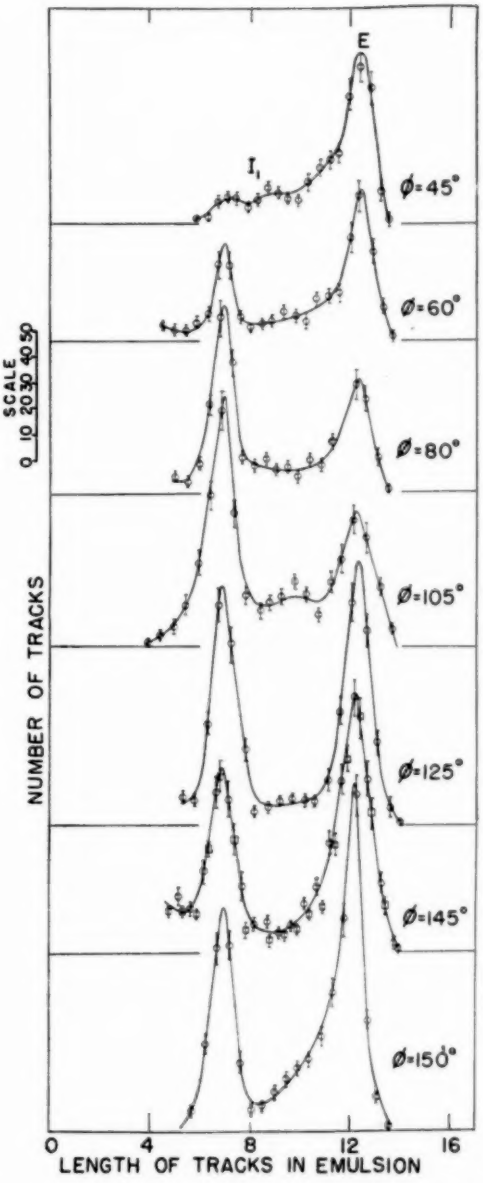

FIG. 3. Range distribution curves for protons scattered by magnesium through various angles ϕ. The curves have been shifted laterally to align the two main peaks, a slight shift being necessary since the recoil energy imparted to the scattering nuclei varies with the angle of scatter. One scale division = 19.6μ.

[19] This measurement should be independent of all such factors as initial inhomogeneity of scattered beam, and characteristic errors in measuring track lengths.

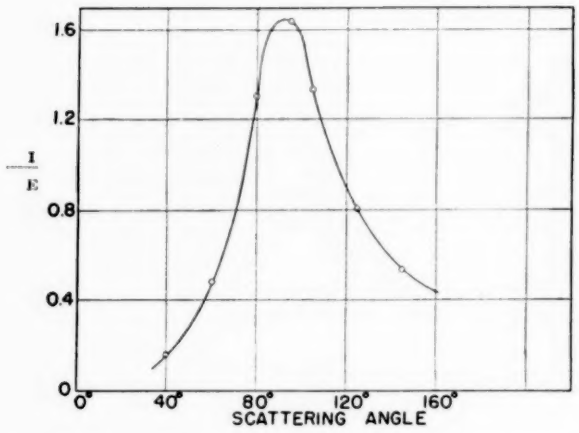

FIG. 4. Relative yield of elastically and inelastically scattered protons as a function of angle for magnesium (run No. III).

of 4°, it is important to know surface and depth conditions in the emulsion. Interference fringes were produced between the surfaces of samples of undeveloped emulsion plates and optically flat glass, using sodium yellow light. It was found that the emulsion surfaces were surprisingly flat except in the immediate vicinity of the natural edges of the plates. Edges along which glass cuts had been made showed no abnormal effects. From plate to plate the emulsion thickness varied between thickness of 30μ to 55μ. At the 4° entrance angle this permits corresponding tracks of maximum length between 400 and 750μ. The finite thickness limits the energy of the protons which can be successfully studied by this method, although considerably thicker emulsion plates are being developed for this purpose.

While it is difficult to estimate the homogeneity of the incident cyclotron beam from available experimental data, a minimum for the mean energy variation can be tentatively considered as ± 0.1 Mev, which is twice the peak voltage across the dees. This is undoubtedly a smaller variation than actually was obtained in the experiments, since variations in the field strength of the cyclotron magnet over the time required for a run are not allowed for.

(2) Precautions relative to scattering angle

To obtain accurately known and reproducible scattering angles care was taken to insure that the center of the ellipse defined by the intersection of the beam of incident protons and the scattering foil was located at the geometrical center of the camera. To prevent reduction in the accuracy of scattering angles due to the effect of the cyclotron's magnetic field on the scattered protons, the camera was located where the field was found to be effectively zero. As an added precaution, the plane of scattering of the camera was vertical, so that in any case any vertical magnetic field could not alter the direction of scattered particles in the plane of scattering.

ADVANTAGES AND DISADVANTAGES OF THE EMULSION TRACK TECHNIQUE

An excellent general survey of the basic advantages and limitations in the use of tracks of nuclear particles in photographic emulsions has been recently presented by Shapiro.[20] Powell and Fertel[21] have demonstrated some of the marked advantages of the technique in the measurement of neutron energies. The undesirable effects of apparent straggling in emulsion track studies have been discussed by Taylor.[22]

Outstanding advantages of the emulsion track technique in nuclear scattering experiments are: (1) Simultaneous exposures can be made at a large number of sharply defined angles in a minimum of time. (2) Both yield and energy distribution of scattered particles are obtained at each scattering angle with the simplest of apparatus. (3) Since the tracks can be seen, random "background" tracks such as those caused near a cyclotron by neutrons, can be recognized as such. (4) Scattered protons of energy as low as 0.8 Mev can be readily detected and their energy estimated. Nothing in the nature of an entrance window is required for emulsions, as in the case of most impulse counters and cloud chambers.

Because of the comparatively slow rate at which track lengths can be measured,[23] several observers have taken part in the track analysis, using three independent microscopes set to the same magnification. In order to make a check

[20] M. Shapiro, Rev. Mod. Phys. **13**, 58 (1941).
[21] Powell and Fertel, Nature **144**, 115 (1939).
[22] H. J. Taylor, Proc. Roy. Soc. **A150**, 382 (1935).
[23] About 200 tracks per hour can be accurately measured for a limited time.

on the personal error involved in such mixed analyses, two observers, working independently on different analyzers, in turn analyzed the same plate (scattering angle 145°). A comparison of these two analyses is included in Fig. 3 in which it is seen that no important variation in curve shape present in the one is absent from the other. The slight difference in total track number is believed due to the fact that one observer counted only those tracks appearing in the portion of the plate seen by the scattering foil, while the other examined the entire plate surface for additional stray tracks.

Results and Discussion

(1) Yield of scattered protons as a function of scattering angle

As a preliminary test of the scattering camera, 6.6-Mev protons were scattered by 0.2-mil platinum foil (run No. I), and the relative numbers (yield) scattered through five different angles were measured. The variation in yield with scattering angle agreed with that predicted for Rutherford scattering, as was expected. Subsequently, the scattering of 6.9-Mev protons by 0.5-mil foils of aluminum and magnesium has been studied and preliminary results presented[9, 10, 14] announcing the detection of inelastic scattering for both elements, and the variation in the relative amounts of inelastic and elastic scattering with angle for the latter.

The apparent straggling effect produced in the photographic emulsion was reduced in the aluminum run (No. II) and in one of the magnesium runs (No. III) by insertion of a suitable thickness of aluminum stopping foils between scattering foil and photographic plates. This had the effect of increasing the resolution between the higher energy groups of scattered protons while cutting off all scattered protons of less than 2.5-Mev energy from the photographic plates. It also shortened the resulting emulsion tracks to such a degree that they could be conveniently examined as units under a microscope using a 10× eyepiece and a 4-mm objective.

Track numbers and lengths have been measured for seven selected plates of run III, and the series of distribution curves so obtained is shown in Fig. 3. The peaks appearing at 12.2 scale divisions are believed to be produced by elastically scattered protons. This conclusion is based on a comparison of the energy of the group of scattered protons of highest energy, and the energy of the incident ones. By use of range energy graphs[24] and the measured lengths of emulsion tracks, the former were found to have a mean energy of 6.87 Mev minus nuclear recoil energy, while from air range measurements the latter were found to have 6.9-Mev energy. The peak at 6.9 scale divisions is seen to appear in all plates of run No. III which have been analyzed so far, and the marked variation with angle of its intensity N_I relative to the intensity N_E of the peak at 9.1 scale divisions is shown in Fig. 4. The ratio N_I/N_E appears to pass through a maximum value for 90° scattering.

The angular distribution of protons scattered by aluminum (run No. II) differs greatly from that predicted for Rutherford scattering. (Fig. 5, curves *B* and *A*, respectively.) While curve *B* includes the total number of protons scattered by aluminum having energies between 3.0 and 6.9 Mev, it actually represents the yield for elastic scattering alone except at large scattering

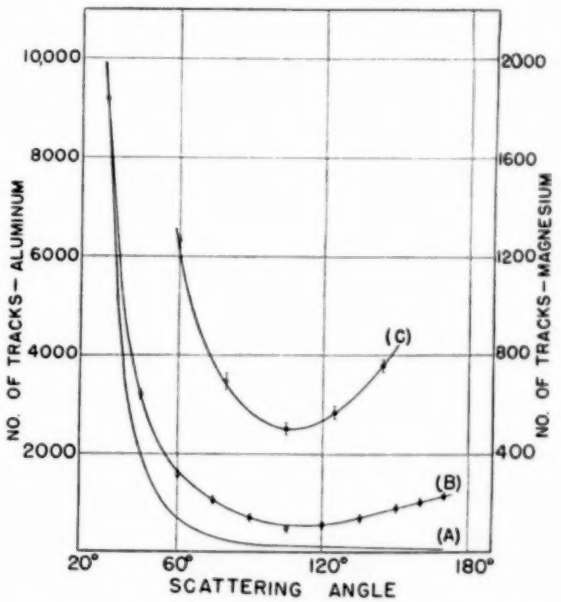

Fig. 5. Yield of elastically scattered protons from aluminum (curve *B*) and magnesium (curve *C*). Curve *A* represents the distribution predicted for Rutherford scattering, and is normalized to curve *B*.

[24] M. S. Livingston and H. A. Bethe, Rev. Mod. Phys. 9, 245 (1937).

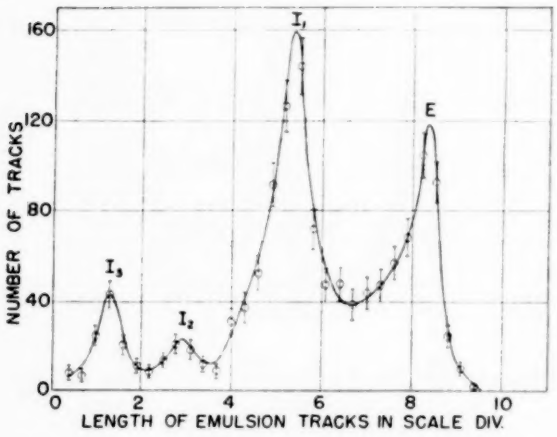

FIG. 6. Range distribution of protons scattered by magnesium for a scattering angle of 95° (run No. IV). One scale division = 39.2μ.

angles, since the one observed group of inelastically scattered protons is small relative to the elastically scattered group, and appears in this run only at scattering angles greater than 145°. The curve for magnesium (Fig. 5, curve *C*) is for elastically scattered protons alone. These curves demonstrate clearly that, exclusive of nuclear collisions in which the scattered particle gives excitation energy to the scattering nucleus, important deviations from Coulomb forces occur in the immediate neighborhood of the nucleus.

There is some evidence in Fig. 3 of unresolved proton groups of comparatively low intensity at about 9.5 and 11.0 scale divisions. An irregularity corresponding to the one at 11.0 scale divisions has been observed in a different experimental study now in progress[25] of proton scattering by magnesium.

In order to observe the distribution of emulsion track lengths over the largest possible energy range, another run (No. IV) was made in which no stopping foils were used between the magnesium scattering foil and the photographic plates. This allowed representative scattered protons of all available energies to reach the photographic emulsions. In Fig. 6 the distribution in emulsion track length of protons scattered through an angle of 95° and measured at one-half of the previous magnification, is shown. The two large peaks previously examined in run No. III are at 5.37 and 8.35 scale divisions, while two further peaks are observed at 2.9 and 1.3 scale divisions. The presence of both of these peaks has been confirmed from the distribution curves of two other plates of the same run. Collection of information concerning their intensity variation with scattering angle is at present in progress.

(2) Excitation energies of magnesium nuclei

An explanation of the series of peaks obtained in Figs. 3 and 6 is that an effect analogous to that found in the Franck-Hertz experiment is occurring when the bombarding protons collide with atomic nuclei. While some of the protons undergo elastic nuclear collisions, others lose a discreet amount of energy to the nucleus. This energy may be considered as exciting the nucleus to a higher quantized energy state, from which it will subsequently revert to its normal state with the emission of gamma-radiation. Hence a measure of the decrease in energy suffered by the groups of inelastically scattered protons should represent directly the excitation energies of the struck nuclei; and these excitation energies and some of their differences should represent possible gamma-ray energies which the nuclei may emit.

The energies of the proton groups were calculated by determining the equivalent proton air ranges from their measured track lengths, and the known stopping powers of the photographic emulsion, stopping, and scattering foils. It is worthy of note, however, that it is incorrect to take the excitation energies as the direct differences between the energy of the elastically scattered group and the energies of the inelastically scattered ones as has been done with earlier results.[10,14] A correction must be made since the recoil energy loss to the nucleus in the inelastic collisions differs from nuclear recoil loss in elastic collisions.[26] Referring to Fig. 6 the proton energies corresponding to peaks E, I_1, I_2, and I_3 are 5.94 Mev, 4.62 Mev, 3.25 Mev, 2.04 Mev, respectively, and the excitation energies corresponding to peaks I_1, I_2, I_3 are 1.37 Mev, 2.80 Mev, 4.07 Mev, respectively, in satisfactory agreement with values of Dicke and Marshall.[25]

[25] R. H. Dicke and J. Marshall, Phys. Rev. **59**, 917 (1941).

[26] I wish to thank Mr. Dicke for developing the necessary correction equations which were used here.

It is only possible with the information available to offer a partial indication as to which of the proton groups I_1, I_2, I_3 is associated with which of the nuclei Mg^{24}, Mg^{25}, Mg^{26}. It is reasonably certain, however, that the group I_1 is produced by Mg^{24}, since at a scattering angle of 90° it is nearly 1.7 times as large as the E group and could scarcely be produced by the other two rarer isotopes. This observation is supported by Henderson's[27] measurement of the gamma-ray energy of radio-sodium in the proposed reaction,

$$Na^{*21} \rightarrow Mg^{24} + \beta + \gamma,$$

in which he finds, by the absorption coefficient method, that the gamma-ray energy has an approximate value of 1.3 Mev which compares with our value of 1.37 Mev. However, from a number of published results, Livingston and Bethe[24] list gamma-rays for this reaction of energies 0.95 Mev, 1.93 Mev, and 3.08 Mev, none of which is closely comparable with the excitation energies or their differences as reported here.

From published studies of the proton groups from the reaction

$$Na^{23} + He^4 \rightarrow Mg^{26} + H^1,$$

Livingston and Bethe[24] have assigned excitation energies to Mg^{26} of 2.2 Mev, 4.0 Mev and 5.0 Mev. Of these, the first mentioned is not observed in our results, while the last value quoted is not in the range of our experiment. However, the group I_3 of measured excitation energy 4.07 Mev might perhaps correspond to the remaining proton group, thus associating this group with Mg^{26}.

[27] M. C. Henderson, Phys. Rev. **48**, 855 (1935).

SEPTEMBER 1, 1941 PHYSICAL REVIEW VOLUME 60

Correction for Nuclear Motion in H_2^+

VIVIAN A. JOHNSON
Purdue University, Lafayette, Indiana

(Received June 30, 1941)

The forced separation of variables usually employed in the quantum-mechanical treatment of molecular problems introduces certain small errors into the wave function. If the exact Hamiltonian is used, energy values can be computed very accurately because first-order errors in a wave function give rise to second-order errors in the energy. The energy of H_2^+ is ordinarily computed by using a separable, approximate Hamiltonian instead of an exact one. From a consideration of the terms which must be added to the approximate Hamiltonian to make it exact, Van Vleck has derived the correction terms needed to reduce the first-order error in the computed energy to a second-order error. The correction term is a function of R, the internuclear distance, and its calculation requires a knowledge of the wave function. In this paper the ground state wave function of H_2^+ is accurately determined over values of R from 1.20 to 2.75 atomic units and a table of the wave function coefficients is given, along with the corresponding energy values. Then, correction terms are calculated for a set of values of R. Including the proper correction term, the total negative energy of H_2^+ for the equilibrium internuclear distance is found to be $1.20472 \pm 0.00001 E_H = 132{,}132 \pm 10$ cm^{-1}. This result is compared with the consequences of certain experimental data.

1. THE PROBLEM

THE usual quantum-mechanical treatment of molecular problems is based upon a forced separation of variables.[1] This introduces certain small errors into the wave function, which, as such, is still as accurate as necessary. Since energy values are subject to much closer check by experimental data, it is desirable to determine energies as accurately as possible. They can be computed very accurately in some cases because first-order errors in a wave function give rise to second-order errors in the energy if the *exact* Hamiltonian is used in calculating the energy. The energy of H_2^+ is computed in the ordinary way by using, not the exact Hamil-

[1] Cf. A. S. Coolidge and H. M. James, J. Chem. Phys. **6**, 730 (1938).

tonian, but the separable, approximate one. From a consideration of the terms which must be added to the approximate Hamiltonian to make it exact, Van Vleck[2] has derived the correction terms needed to reduce the first-order error in the computed energy due to total neglect of the motion of the nuclei to a second-order error due to carrying out the computation with approximate wave functions. The correction term, denoted by $P_{nn}+Q_{nn}+S_{nn}$, is a function of R, the internuclear distance. The potential energy at each value of R is obtained by adding this correction to the energy value of the corresponding fixed-nuclei solution. For infinite separation this correction becomes that required to convert the fixed- into the free-nuclei problem, hence it may be termed "the correction for nuclear motion." In this paper the ground state wave function of H_2^+ is accurately determined over values of R from 1.20 to 2.75 atomic units and the corresponding corrections for nuclear motion evaluated. A corrected value of the energy of H_2^+ for equilibrium internuclear distance is obtained and compared with certain experimental results.

2. Calculation of the Wave Function

The calculation of the wave functions of H_2^+ has been discussed in numerous papers in recent years;[3-11] but, due to the difficulties of calculation described below, the various authors have calculated only the energy values and not the wave function itself. Hence the first step in calculating the correction for nuclear motion is to make an accurate determination of the ground state wave function.

If elliptical coordinates, ξ, η, φ, are inserted in the Schrödinger equation, the latter becomes separable and the wave function for the ground state may be written:

$$\Psi(\xi, \eta, \varphi)=\frac{C}{(2\pi)^{\frac{1}{2}}}X(\xi)\,Y(\eta), \tag{1}$$

where C is the normalization constant. $Y(\eta)$ and $X(\xi)$ are defined by the differential equations:

$$\frac{d}{d\eta}(1-\eta^2)\frac{dY}{d\eta}+(\lambda^2\eta^2+\mu')\,Y=0, \tag{2}$$

$$\frac{d}{d\xi}(1-\xi^2)\frac{dX}{d\xi}+(\lambda^2\xi^2-2R\xi+\mu')X=0, \tag{3}$$

in which $\lambda^2=-E'R^2/2$, E' being the electronic part of the energy.

The solution of (2) is given by

$$Y(\eta)=1+a_2(\lambda)P_2(\eta)+a_4(\lambda)P_4(\eta)+a_6(\lambda)P_6(\eta)+\cdots \tag{4}$$

where, in order that the series may converge, the a_l must satisfy the relation:

$$a_{l-2}\lambda^2\frac{l(l-1)}{(2l-3)(2l-1)}+a_l\left[\mu'-l(l+1)+\lambda^2\left\{\frac{(l+1)^2}{(2l+1)(2l+3)}+\frac{l^2}{(2l+1)(2l-1)}\right\}\right]+a_{l+2}\lambda^2\frac{(l+1)(l+2)}{(2l+3)(2l+5)}=0.$$

So that the above equation may be satisfied by values of a_l other than zero, μ' and λ^2 must satisfy a functional relation, given in continued fraction form by Wilson[4] and solved in series form (accurate to the sixth decimal place) by Sandeman:[9]

$$-\mu'=\frac{\lambda^2}{3}+\frac{2\lambda^4}{3^3\cdot5}+\frac{4\lambda^6}{3^5\cdot5\cdot7}-\frac{26\lambda^8}{3^7\cdot5^3\cdot7}-\frac{92\lambda^{10}}{3^9\cdot5^2\cdot7\cdot11}-\frac{513988\lambda^{12}}{3^{10}\cdot5^5\cdot7^3\cdot11\cdot13}+\frac{2894282\lambda^{14}}{3^{12}\cdot5^6\cdot7^3\cdot11\cdot13}\cdots. \tag{5}$$

[2] J. H. Van Vleck, J. Chem. Phys. **4**, 327 (1936).
[3] Ø. Burrau, Kgl. Danske, Vid. Selsk. **7**, No. 14 (1927).
[4] A. H. Wilson, Proc. Roy. Soc. **A118**, 617, 637 (1928).
[5] P. M. Morse and E. C. G. Stueckelberg, Phys. Rev. **33**, 932 (1929).
[6] E. Teller, Zeits. f. Physik **61**, 458 (1930).
[7] E. A. Hylleraas, Zeits. f. Physik **71**, 739 (1931).
[8] G. Jaffe, Zeits. f. Physik **87**, 535 (1934).
[9] I. Sandeman, Proc. Roy. Soc. Edinburgh **55**, 72 (1935).
[10] W. G. Baber and H. R. Hasse, Proc. Camb. Phil. Soc. **31**, 564 (1935).
[11] S. K. Chakravarty, Phil. Mag. **28**, 423 (1939).

TABLE I. *Wave function coefficients and energy values.*

λ	R	a_2	a_4	a_6	b_1	b_2	b_3	C	E'*	E*
1.0	1.214301	0.114518	0.001978	0.0000137	0.008496	0.0003706	0.0000411	3.612652	−2.712737	−1.065698
1.1	1.366077	.139388	.002919	.0000243	.010137	.0003908	.0000406	3.660361	−2.593552	−1.129506
1.2	1.523336	.166929	.004159	.0000410	.011831	.0004032	.0000392	3.723734	−2.482167	−1.169259
1.3	1.685909	.197207	.005770	.0000663	.013559	.0004086	.0000373	3.802924	−2.378365	−1.192061
1.4	1.853595	.230283	.007815	.0001035	.015301	.0004077	.0000348	3.898359	−2.281847	−1.202863
1.5	2.026162	.266212	.010364	.0001565	.017039	.0004014	.0000323	4.010611	−2.192272	−1.205184
1.6	2.203349	.305038	.013487	.0002306	.018757	.0003906	.0000294	4.140736	−2.109276	−1.201567
1.7	2.384868	.346787	.017253	.0003317	.020438	.0003762	.0000267	4.292105	−2.032493	−1.193872
1.8	2.570407	.391465	.021719	.0004674	.022068	.0003590	.0000239	4.459978	−1.961558	−1.183471
1.9	2.759633	.439049	.026927	.0006465	.023634	.0003399	.0000214	4.653078	−1.896115	−1.171381
1.483559	1.997466**	0.260107	0.009908	0.0001465	0.016754	0.0004028	0.0000328	3.991018	−2.206537	−1.205268

* E' and E are given in terms of $E_H = 109{,}679\ \text{cm}^{-1} = 13.530$ ev.
** Equilibrium internuclear distance.

The solution of (3) is written

$$X(\xi) = e^{-\lambda\xi}\left(\frac{2}{\xi+1}\right)^{\rho}\left\{1+b_1(\lambda)\frac{\xi-1}{\xi+1}+b_2(\lambda)\left(\frac{\xi-1}{\xi+1}\right)^2+b_3(\lambda)\left(\frac{\xi-1}{\xi+1}\right)^3+\cdots\right\}, \tag{6}$$

where $\rho = 1-(R/\lambda)$. In order that the series may converge, b_m must satisfy the relation

$$b_{m+1} = -u_m b_m + v_{m-1} b_{m-1}, \quad b_{-1} = 0, \tag{7}$$

where

$$-u_m = \frac{2m^2+2m(\rho+2\lambda)+(\rho+2\rho\lambda+\lambda^2+\mu')}{(m+1)^2}, \quad -v_{m-1} = (m-1+\rho)^2/(m+1)^2.$$

So that (7) may be satisfied by values of b_m other than zero, μ', λ, and ρ (or R) must be related in the manner indicated by the continued fraction:

$$-u_0 = \cfrac{v_0}{u_1+\cfrac{v_1}{u_2+\cfrac{v_2}{u_3+\cdots}}}. \tag{8}$$

In theory it is possible to eliminate μ' between (5) and (8) to obtain a relation between λ and R;[10,11] in practice it is extremely difficult to determine an algebraic relation between λ and R sufficiently accurate to yield reliable values for the wave function coefficients. In the present work this calculation has been done numerically to insure maximum accuracy; for an arbitrary value of λ, μ' was found from (5), and then (8) was solved for the corresponding unique value of ρ (and hence R). From these values (all accurate to the sixth decimal place), corresponding values of a_l, b_m, C, and the energies E' and $E[=E'+(e^2/R)]$ were determined with like accuracy. Table I gives these results over a range of values of λ (or R); the last row gives results for the equilibrium value of R.

The value of the energy for the equilibrium value of R is exactly equal to that found by Hylleraas.[7] Sandeman[9] calculated a somewhat smaller absolute value. His result probably is slightly in error because the empirical formula relating λ and R, from which he obtained the energy minimum by the appropriate differentiation, was obtained from pairs of values of λ and R which fail to give agreement in Eq. (8) by about two percent.

The pairs of values of λ and R tabulated in Table I give rise to the empirical relation:

$$R = 0.0099234+0.9302959\lambda+0.2461946\lambda^2+0.0449322\lambda^3-0.0176366\lambda^4+0.0006485\lambda^5 -0.0000972\lambda^6+0.0000397\lambda^7\cdots. \tag{9}$$

3. Calculation of $P_{nn}+Q_{nn}+S_{nn}$ and Discussion of Results

Van Vleck's[2] expression for S_{nn}, which represents the energy difference due to the fact that the center of gravity of the molecule does not exactly coincide with the center of gravity of the nuclei,

becomes for H_2^+:

$$\frac{S_{nn}}{E_H}=-\frac{2}{M_P R^2}\int\frac{1}{\xi^2-\eta^2}\Psi\left\{\frac{\partial}{\partial\xi}(\xi^2-1)\frac{\partial\Psi}{\partial\xi}+\frac{\partial}{\partial\eta}(1-\eta^2)\frac{\partial\Psi}{\partial\eta}\right\}d\tau$$
$$=\frac{C^2R}{4M_P}\left[\int_{-1}^{1}Y^2d\eta\int_{1}^{\infty}(\xi^2-1)\left(\frac{\partial X}{\partial\xi}\right)^2d\xi+\int_{1}^{\infty}X^2d\xi\int_{-1}^{1}(1-\eta^2)\left(\frac{\partial Y}{\partial\eta}\right)^2d\eta\right], \tag{10}$$

where M_P = mass of proton, E_H = ionization potential of hydrogen.

The corresponding expression for $P_{nn}+Q_{nn}$, which may be qualitatively described as representing coupling between vibrational and electronic motion, is

$$\frac{P_{nn}+Q_{nn}}{E_H}=\frac{2}{M_P}\int\left(\frac{\partial\Psi}{\partial R}\right)^2d\tau-\frac{4}{M_P R}\int\frac{1}{\xi^2-\eta^2}\frac{\partial\Psi}{\partial R}\left\{\xi(\xi^2-1)\frac{\partial\Psi}{\partial\xi}+\eta(1-\eta^2)\frac{\partial\Psi}{\partial\eta}\right\}d\tau$$
$$+\frac{2}{M_P R^2}\int\frac{\xi^2+\eta^2-1}{\xi^2-\eta^2}\left\{(\xi^2-1)\left(\frac{\partial\Psi}{\partial\xi}\right)^2+(1-\eta^2)\left(\frac{\partial\Psi}{\partial\eta}\right)^2\right\}d\tau$$
$$=\frac{C^2R^3}{4M_P}\int_{-1}^{1}\int_{1}^{\infty}\left[\frac{\partial}{\partial R}(XY)\right]^2(\xi^2-\eta^2)d\xi d\eta$$
$$-\frac{C^2R^2}{2M_P}\int_{-1}^{1}\int_{1}^{\infty}\frac{\partial}{\partial R}\{XY\}\left\{Y\xi(\xi^2-1)\frac{\partial X}{\partial\xi}+X\eta(1-\eta^2)\frac{\partial Y}{\partial\eta}\right\}d\xi d\eta$$
$$+\frac{C^2R}{4M_P}\int_{-1}^{1}\int_{1}^{\infty}(\xi^2+\eta^2)\left\{Y^2(\xi^2-1)\left(\frac{\partial X}{\partial\xi}\right)^2+X^2(1-\eta^2)\left(\frac{\partial Y}{\partial\eta}\right)^2\right\}d\xi d\eta-\frac{S_{nn}}{E_H}. \tag{11}$$

The expression defined in Eq. (10) has been evaluated in a straightforward manner for a series of values of λ. The evaluation of expression (11) involves the calculation of the derivatives of the coefficients a_l and b_m and of λ and ρ with respect to R.[12] The appropriate derivatives have been calculated for different values of λ by use of the Gregory-Newton interpolation formula for derivatives of tabulated functions. Otherwise the evaluation of (11) involves only lengthy, but straightforward, integrations. Figure 1 shows the variation of S_{nn}, $P_{nn}+Q_{nn}$, and $P_{nn}+Q_{nn}+S_{nn}$ with internuclear distance. The total correction for nuclear motion at the equilibrium distance is $0.00055\pm0.00001\ E_H$ ($60\ \text{cm}^{-1}=0.0075$ ev). Van Vleck[1] has estimated this quantity as $114\ \text{cm}^{-1}=0.014$ ev.

By combining the correction for nuclear motion with the value of the energy at equilibrium internuclear distance given in Table I, the total negative energy of H_2^+ becomes, for this value of R,

$$W(H_2^+)=1.20472\pm0.00001E_H$$
$$=132{,}132\pm10\ \text{cm}^{-1} \tag{12}$$
$$=16.300\pm0.001\ \text{ev}.$$

This value now can be compared with the results of experiment.

The total energy of H_2 equals twice the ionization energy of the H atom plus the dissociation energy of H_2. Beutler and Junger[13] have obtained a direct experimental value of the dissociation energy:

$$D(H_2)=36{,}116\pm6\ \text{cm}^{-1}.$$

With this value, the energy of H_2 becomes

$$W(H_2)=2(109{,}679)+36{,}116 \tag{13}$$
$$=255{,}474\pm6\ \text{cm}^{-1}.$$

[12] The normalization constant C is also a function of R, but calculation shows that terms involving $\partial C/\partial R$ are negligible compared to the others; hence such terms are omitted in Eq. (11).

[13] H. Beutler and H. O. Junger, Zeits. f. Physik **101**, 304 (1936).

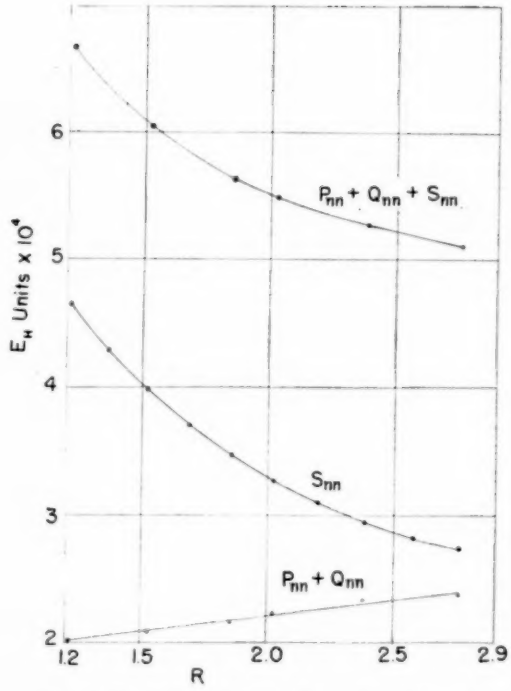

FIG. 1. Variation of $P_{nn}+Q_{nn}+S_{nn}$, S_{nn} and $P_{nn}+Q_{nn}$ with internuclear distance.

The ionization energy of H_2 can now be calculated, for the total energy of H_2 equals the ionization energy of H_2 plus the energy of H_2^+ minus the zero-point vibrational energy of H_2^+. By extrapolation from a singlet series of H_2, Richardson[14] has obtained for the zero-point energy the value 0.1399 ± 0.0007 ev; Sandeman's theoretical work gives 0.1390 ev. The computations of this paper lead to the value

$$0.1389 \text{ ev} = 1126 \text{ cm}^{-1} \quad \text{(error not exceeding } 10 \text{ cm}^{-1}\text{)}. \quad (14)$$

[14] O. W. Richardson, Proc. Roy. Soc. **A152**, 503 (1935); *Molecular Hydrogen and Its Spectrum* (Yale University Press, New York, 1934), p. 158.

This value of the zero-point energy and the value of the energy of H_2^+ given in (12) give for the ionization energy of H_2:

$$I(H_2) = 255{,}474 - 132{,}132 + 1126 \quad (15)$$
$$= 124{,}468 \pm 20 \text{ cm}^{-1}.$$

Beutler and Junger, noting that the ionization energy of H_2 cannot be measured with the same accuracy as the dissociation energy, have obtained the experimental value

$$I(H_2) = 124{,}427 \pm 10 \text{ cm}^{-1}.$$

The small discrepancy may indicate that the probable error has been underestimated in one or both cases.

The dissociation energy of H_2^+ equals the energy of H_2^+ minus the zero-point vibrational energy of H_2^+ minus the ionization energy of the H atom. Using the theoretical values (12) and (14), one obtains:

$$D(H_2^+) = 132{,}132 - 1126 - 109{,}679 \quad (16)$$
$$= 21{,}327 \pm 20 \text{ cm}^{-1}.$$

This result cannot be directly compared with experiment because direct observations on the H_2^+ spectrum are completely lacking. The experimental value, $21{,}366\pm15$ cm^{-1}, given by Beutler and Junger is a combination of the ionization and dissociation energies of H_2; hence the small discrepancy between calculated and experimental values of $I(H_2)$ appears again here.

The author wants to thank Dr. Hubert M. James for suggesting this problem and for many discussions concerning its solution and Dr. K. Lark-Horovitz for his encouragement during the progress of the work.

The Multiple Scattering of Fast Electrons

N. L. Oleson,* K. T. Chao† and H. R. Crane
The Harrison M. Randall Laboratory, University of Michigan, Ann Arbor, Michigan

(Received July 11, 1941)

An extensive cloud-chamber investigation of the scattering of fast electrons (3–11 Mev) by foils of various elements has been completed. The foils were of such thickness that the resultant average deflection was due chiefly to many deflections through small angles. This fact makes possible a comparison with two recent theories of multiple scattering. The results indicate that, for elements at either end of the atomic number scale, the scattering is less than predicted by theory. For elements of intermediate atomic numbers, there is good agreement with theory. An attempt was made to detect the effect of crystal size on scattering. The results were negative within our limits of error, and, if such an effect exists, it must be small.

Introduction

ONE important aspect of the problem of scattering of electrons is the scattering through extremely small angles. This usually means scattering in which the electrons pass through that part of the atomic field which is partially screened by the orbital electrons. So far, we have no method of studying this kind of scattering as individual events, because the deflections are far too small. Instead, we must attack the problem by observing the result of multiple deflections. The usual method is to allow electrons of known energy to pass through a lamina of solid material and to observe the difference in direction of incidence and emergence for each electron; the angle measured being in each case the result of thousands of individual deflections. The theory of multiple scattering begins with an assumption as to the elementary scattering law (which is complicated by the screening) and from that point on the problem is one of statistically summing the many deflections. Naturally, it is only with the aid of an accurate treatment of this statistical problem that a comparison of the experimental results with theory can be considered to be a good test of the laws of interaction between atoms and rapidly moving electrons at large distances from the nucleus. Recently, two theories[1,2] of multiple scattering have been published in which the statistics has been sufficiently developed to allow a significant comparison of theory with experiment. These will be compared with our experimental results.

Experimental Procedure

Apparatus

The source of electrons was Li^8, obtained by the reaction

$$Li^7+D^2\rightarrow Li^8+H^1.$$

The Li^8 disintegrates with a half-life of 0.8 second according to the reaction

$$Li^8\rightarrow Be^8+e^-$$

giving a beta-ray spectrum whose upper limit is 12 Mev.[3]

The deuterons were accelerated by means of the high voltage vacuum tube apparatus, which has been described elsewhere.[4] Because of the short half-life it was necessary to prepare the Li^8 just before each expansion of the cloud chamber.[5] A target of lithium metal was bombarded with 0.8-Mev deuterons for 2 seconds, then about $\frac{1}{2}$ second was allowed for the cloud chamber to be cleared of ions before the expansion occurred. The high voltage tube and the cloud chamber were controlled by the same motor-driven contact system, so that the cycle repeated automatically. The electrons emerged from the

* Now at the United States Coast Guard Academy, New London, Connecticut.

† Present Address: Institute of Radium, National Academy of Peiping, Shanghai, China.

[1] E. J. Williams, Proc. Roy. Soc. **169**, 531 (1939); Phys. Rev. **58**, 292 (1940).

[2] S. Goudsmit and J. L. Saunderson, Phys. Rev. **57**, 24, 552 (1940); Phys. Rev. **58**, 36 (1940).

[3] D. S. Bayley and H. R. Crane, Phys. Rev. **52**, 604 (1937).

[4] H. R. Crane, Phys. Rev. **52**, 11 (1937).

[5] H. R. Crane, Rev. Sci. Inst. **8**, 440 (1937).

vacuum tube through a thin aluminum window, and were allowed to enter the cloud chamber through another aluminum window in its side wall, falling perpendicularly upon the scattering lamina, as shown in Fig. 1. The electrons were roughly selected as to energy by the appropriate placing of lead slits between the tube and the cloud-chamber window, making use of that part of the magnetic field which extends outside the chamber. To reduce the possibility of confusion, the intensity of the electron source was adjusted so that, on the average, only about three tracks appeared on each photograph.

For use later in considering possible errors due to geometry, it is necessary to state the exact dimension of the cloud chamber. It is used in a horizontal position, is 15 cm in diameter, and has a total depth of 5 cm when expanded. The collimated light beam illuminates a slice of the chamber 2.5 cm in depth, located in the center with respect to the top plate and floor of the chamber. The scattering lamina was attached to the top glass plate of the chamber, and extended well beyond the illuminated part of the chamber, so that there was no possibility of photographing tracks of electrons which passed under the lamina. The window through which the electrons entered was 8 mm high and 2.5 cm long, and was at a distance of about 30 cm from the lithium source. This means that the incident electron paths were very nearly parallel to the plane of the chamber, and that they struck the scattering lamina at its center. Photographs were taken from a point directly above the chamber with a Sept 35 mm camera, in the vertical position.

Criteria for selecting and measuring tracks

Only those tracks were included in the data which satisfied the following criteria: (1) The incident track must make an angle not greater than 15 degrees with the normal to the scatterer, measured in the plane projection. (2) The incident track must be clear and sharp over a distance of at least 5 cm and to within 5 mm of the scatterer. (3) The emergent track must have a visible length of not less than 7 cm and extend to within 5 mm of the scatterer. The illuminated portion of the chamber is approximately 2.5 cm deep and the point of scattering is located at the middle of the illuminated region. (See Fig. 1.) This means that the vertical component of the actual scattering is limited to $2.5/2\times7\backsimeq10$ degrees. (4) The track must not be visibly distorted by scattering in the gas of the cloud chamber.

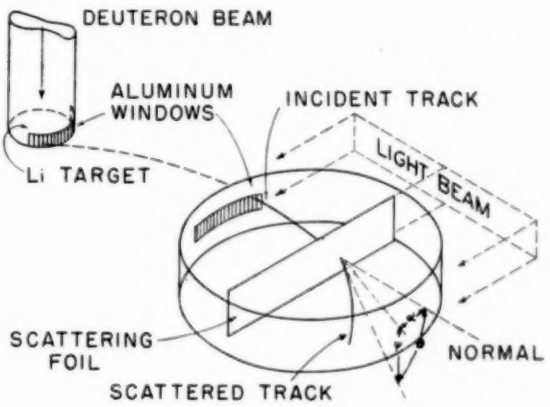

FIG. 1. Arrangement of apparatus.

Measurement of tracks

Because of the large number of scattering angles which were to be measured, we found it necessary to devise a rapid method of measurement. A set of circles, in steps of $\frac{1}{2}$ cm, was engraved on a piece of transparent celluloid about 6×8 inches in size. This was then cut in the center, on a common radius of the circles. To measure the incident part of the track, a circle was fitted to the projected image track as shown in Fig. 2. The radius of curvature was recorded, and a line drawn along the edge of the celluloid at AA. This line is perpendicular to the track at the scattering foil. A similar measurement of the other half of the track is made with the other half of the celluloid, drawing a line along edge BB. The angle between the two lines gives the angle of scattering; also both radii of curvature are obtained. The average of the two radii is used, and this automatically takes care of the energy loss within the scattering material. This loss is appreciable only in the carbon scatterer, however.

Scattering foils

The scattering foil in each case was made of such a thickness that the average angle of scattering was roughly 10 degrees. A greater

thickness (and greater average angle of scattering) would have made the errors due to geometrical limitations of the cloud chamber too great. On the other hand, thinner scatterers than those used would have given rise to large relative errors in the measurements of the angles. All the scattering foils used had, therefore, about the same scattering power, or, the number of atoms per sq. cm area times Z^2 was about constant.

Theory

Full descriptions of the several theories will not be attempted here, but only enough of each will be given to enable the reader to understand clearly how we have used the theory.

The Williams theory

In the multiple scattering theory of E. J. Williams, the distribution of the horizontal projection of the resultant angle of scattering (angle α in Fig. 1) due to individual deflections between ϕ_1, and $\phi_{\min}$ is taken to be Gaussian.

ϕ_1 is defined as that angle such that, on the average, each electron experiences one deflection greater than ϕ_1 in passing through the foil. $\phi_{\min}$ is an effective cut-off angle, due to the shielding of the nuclear field by the orbital electrons, the value of which is obtained by using the Fermi-Thomas distribution of electrons in the atom. A correction for the effect of individual deflections greater than ϕ_1 is applied later, and its effect on the distribution curve is to broaden the Gaussian part and to add a tail, which is usually referred to as the "single scattering tail." Since the average angle of scattering, for a monochromatic electron beam, varies inversely as $H\rho$, it is convenient to make plots in which the abscissa is $H\rho\alpha$, as in Figs. 3 to 6. The angle of scattering of *each electron* is multiplied by its own $H\rho$ value. In this way, a group of electrons having a wide range in $H\rho$ may be placed on the same plot, for the purpose of comparison with theory.

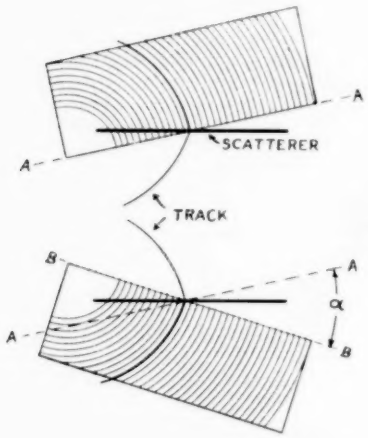

FIG. 2. Method of measuring curvature of tracks.

Williams' formula is

$$(H\rho\alpha)_{Av}=0.88A^{\frac{1}{2}}[(9.41+\log A-0.67\log Z)^{\frac{1}{2}}+1.81]\cdot 10^5 \text{ gauss centimeters degrees,} \quad (1)$$

where A is a parameter characterizing the scatterer given by

$$A=0.151\sigma Z^2/M, \quad (2)$$

where M is the atomic weight of the scatterer of atomic number Z. σ is the superficial density of the scatterer in grams per square centimeter. $H\rho$ is the product of the magnetic field intensity and the average radius of curvature of the electron in the field.

The Goudsmit and Saunderson theory

The theory of Goudsmit and Saunderson does not divide the individual deflections into regions above and below a certain angle, such as ϕ_1, in the Williams theory, but, by means of standard methods of the calculus of probability, the whole range is treated at once. $(H\rho\alpha)_{Av}$ is not given by a formula analogous to Williams' formula, because the momentum dependence upon $\bar{\alpha}$ is not linear and explicit. However, the exact values of $(H\rho\alpha)_{Av}$ for a large number of different scatterers and energies have been computed by Goudsmit and Saunderson,[6] and, by making interpolations of values given in their table, $(H\rho\alpha)_{Av}$ is easily obtained for any case which has so far been tried experimentally. The scattering distribution is essentially Gaussian provided $\bar{\alpha}$ is not large ($\sim$10 degrees). The corresponding average involving the total angle of scattering θ (Fig. 1) is obtained by the same procedure. In this case, however, the variation with energy is found to be small for the range of energies dealt with in this investigation and can be represented

[6] S. Goudsmit and J. L. Saunderson, Phys. Rev. **57**, 24 (1940), Table III.

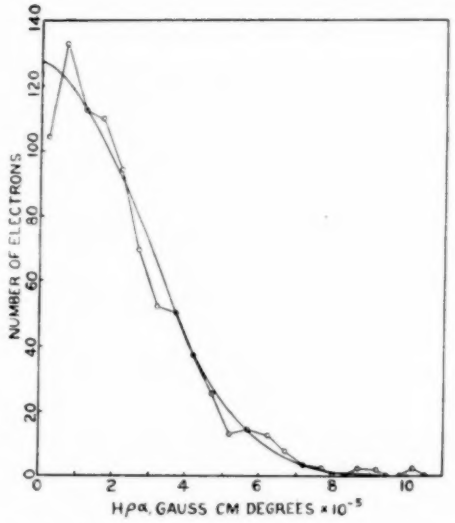

FIG. 3. Scattering of electrons by C, 0.82 g/cm².

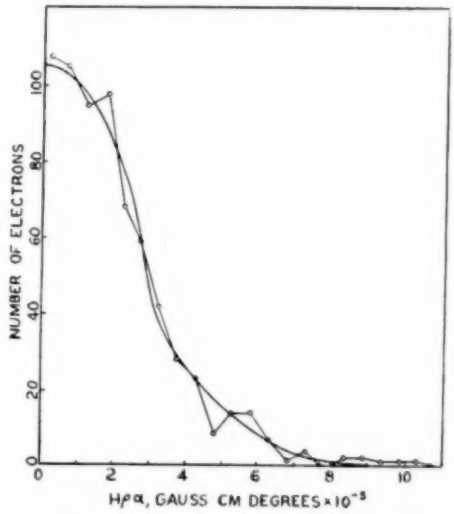

FIG. 4. Scattering of electrons by Cd, 0.111 g/cm².

to a good approximation by the formula

$$(H\rho\theta)_{Av}=1.70A^{\frac{1}{3}}(5.60-\tfrac{1}{3}\log Z+\tfrac{1}{2}\log A)^{\frac{1}{2}}\cdot 10^{5}$$
gauss centimeters degrees. (3)

Scattering by orbital electrons

To account for the scattering due to collisions with the orbital electrons, we have assumed that each orbital electron scatters as if it were a nucleus of atomic number one. Since there are Z electrons per atom, we have simply to substitute Z^2+Z for Z^2 in the theoretical formulas. In all the theoretical values quoted by us, this substitution has been made.

The effect of crystal structure upon multiple scattering

The scattering materials used in most of the experiments so far have been of polycrystalline structure (metals, for example). Also, an important part of the multiple scattering is due to individual angles of deflection which are of the same order of magnitude as the angle between maxima in the crystal diffraction pattern for electrons of the same energy. Wheeler[7] has suggested that, in view of this fact, the scattering may not be independent of the crystalline structure, and that some of the second-order effects, such as extinction of the scattered beam by rescattering back into the original direction, may have an influence upon the total scattering, as is well known in the case of x-ray diffraction. Some preliminary estimates of the magnitude of the effect have been made by Wheeler. It is interesting to note two ways in which the diffraction of electrons differs from that of x-rays: (1) Coherence exists only over the distance between inelastic collisions, which is about 10^{-5} cm in carbon at this energy, for example. (2) The scattering power of each atom is so great, that, before many crystal planes have been traversed, all the intensity has disappeared from the original beam. The participation of such a small number of planes in the coherent scattering process means that the maxima are broad, and the effect of extinction is thereby lessened. The first of these limitations was pointed out to the authors by Professor Wheeler, and the second by Professor Wigner.

[7] J. A. Wheeler, Phys. Rev. **57**, 352A (1940).

ERRORS AND CORRECTIONS

Geometrical limitations in the cloud chamber

It has already been mentioned that a track was included in the data, only if the emergent portion had a length of at least 7 cm. Since the illuminated section of the chamber has a depth of 2.5 cm, such a criterion is equivalent to imposing an upper limit of about 10 degrees on the vertical component of the scattering angle. In the region of multiple scattering, where the distribution is approximately Gaussian, such a limitation would not affect the shape of the

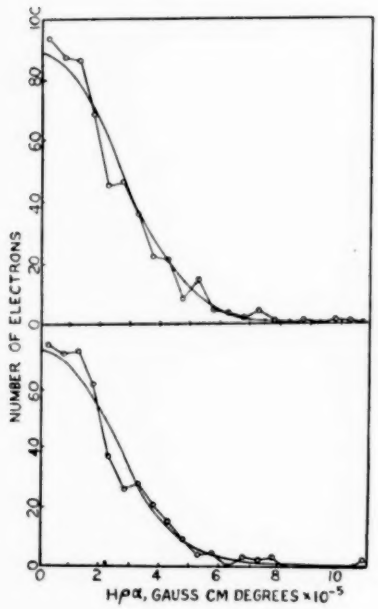

FIG. 5. Scattering of electrons by Cu and Fe. Upper curve Cu, 0.174 g/cm². Lower curve Fe, 0.173 g/cm².

distribution in α, the projected angle of scattering, whereas, in the region of the single scattering tail, this restriction has the effect of reducing the single scattering tail and, hence, the contribution of single scattering to the total scattering. Williams takes account of this limitation and gives an approximate formula for calculating the reduction in the value of $(H\rho\alpha)_{Av}$.[8] Goudsmit and Saunderson correct for this effect by a method which amounts to interpolating between the theoretical values for two extremes: an infinitely thin chamber, and an infinitely thick chamber.[9] Both of these cases can be evaluated theoretically, and the difference between them is not large. In all the theoretical values quoted by us, these corrections have been included.

Scattering in the gas

The directions of the incident and emergent tracks are obtained by fitting portions of circles to them; therefore, the direction obtained represents an average direction along its length, which is about 7 cm. The electron actually suffers small angle multiple scattering along its path in the gas, so that, if there were no scattering at all in the solid scatterer, we would still observe a small angular spread, due to the method of measurement and the scattering in the gas. The latter angles are added in random direction to those produced by the solid scatterer, so the measured result is the square root of the sum of the squares of the average angles produced by the solid scatterer and by the gas. In fact, the gas can simply be considered as an addition to the thickness of the solid lamina. This correction has been calculated, and is small enough to be neglected, for all the scatterers used in the present work. For very thin scatterers, such as the 0.0025-cm aluminum used by Slawsky and Crane,[10] the correction is important, as Williams has pointed out.

Error in measurement of energy

The error in the measurement of the curvature of a track is due mainly to scattering in the gas, which makes it depart from circularity, or changes its apparent radius of curvature. Williams has derived a formula for this effect, and for tracks 7 cm long, in air at NTP, it reduces to $\rho/\rho_s=48/H$, where ρ is the radius of curvature, due to the magnetic field alone, and ρ_s is that due to scattering by the gas alone. The error for individual tracks in our measurements, where H ranges between 1260 and 2520 gauss, is, according to the above, about 4 percent at 1260 gauss, and 2 percent at 2520 gauss. The average angle in the multiple scattering by the lamina varies inversely as the first power of the energy, so the error due to the above cause will remain symmetrical in the final result. Therefore, the estimated error, at 1260 gauss, is $4/\sqrt{n}$ percent, where n is the number of

[8] The formula referred to is Eq. (13) in Williams second paper for the case $\psi<\phi_2$, where ψ is the upper limit imposed by the cloud-chamber geometry on the vertical angle ($\sim$10 degrees) and ϕ_2, the angle corresponding to the intersection of the Gaussian distribution with the single scattering curve. (See Fig. 1 of Williams' first paper) $\phi_2>25°$ for the scattering foils used in this investigation.

[9] The actual $(H\rho\alpha)_{Av}$ should lie between $(H\rho\theta)_{Av}$ and $(H\rho\alpha)_{Av}$ obtained from interpolation of their tables, and should be closer to $(H\rho\theta)_{Av}$. This follows from the fact that, if the upper limit on the vertical angle is small, that is, only a very thin horizontal slice of the cloud chamber being considered, the actual $(H\rho\alpha)_{Av}$ should be given by $(H\rho\theta)_{Av}$ interpolated. On the other hand, if all vertical angles are possible, then the actual value is given by $(H\rho\alpha)_{Av}$ interpolated. As the upper limit on the vertical angle is about 10 degrees, the condition of a thin slice is realized. Therefore, the actual value should be a little above the interpolated $(H\rho\theta)_{Av}$ and is given to a good approximation by Eq. (3).

[10] M. M. Slawsky and H. R. Crane, Phys. Rev. **56**, 1203 (1939).

tracks in the group (about 400). This is in the neighborhood of 0.2 percent.

Energy loss inside the scatterer

For each of our tracks, the arithmetic average of the ingoing and outgoing curvatures was used, since the energy difference was small, and one can, therefore, assume a linear decrease. This automatically takes care of the effect of energy loss, because, in the multiple scattering, the average angle depends linearly upon the energy.

Path length in the scatterer

Williams[2] and Rose[11] have called attention to the fact that, in scattering measurements, a correction should be made for path length in the scatterer. The path length[12] is approximately

$$t(1+\tfrac{1}{2}\bar{\theta}^2),$$

where t is the actual foil thickness, and $\bar{\theta}$ is the average angle of scattering. In terms of the average projected angle $\bar{\alpha}$ this would become

$$t(1+\bar{\alpha}^2)$$

if all angles concerned are small. This represents a minimum correction, since it assumes that all the tracks are incident upon the scatterer exactly perpendicularly. Actually, the tracks included in our data made angles up to 15 degrees with the normal as measured in the horizontal plane projection. The spread in angle in the vertical plane was much smaller, due to the geometry of the slit system through which the electrons passed. All facts considered, it seems fair to take $t(1+2\bar{\alpha}^2)$ as the average path length. Thus the correction factor for the average projected angle of scattering is approximately $(1+\bar{\alpha}^2)$.

Personal errors in measurement

If the errors in matching the circles to the tracks and measuring angles were random, or even symmetrical as to + and −, the net effect would be very small. Unfortunately there is no assurance that this is so, since the person measuring may have a tendency to make an error in a given direction. One can only guess at the amount of the error introduced. We believe that a generous estimate of the probable error in the final result due to such a systematic effect would be 3 percent.

Calibration of instruments

The errors involved in the calibration of the magnetic field, the size of the projected image, etc., combined, are expected to contain a probable error of about 2 percent.

Combined effect of all errors

In consideration of all the sources of error mentioned above we believe that a generous estimate of the probable error on our results is ±5 percent.

Results

Experimental results, with the values calculated by means of the two theories, are given in Tables I and II. The theoretical values contain the necessary correction for the path length in the scattering lamina, the correction for scattering by the orbital electrons and the effect of cloud-chamber geometry (in the case of the Williams theory). Typical examples of plots of the data obtained together with Gaussian curves[13] are shown in Figs. 3 to 7. Plots of all the curves obtained are not reproduced here because they would add little or nothing to the information contained in the accompanying tables. All the plots are Gaussian in shape, to within the experimental accuracy, as is to be expected.

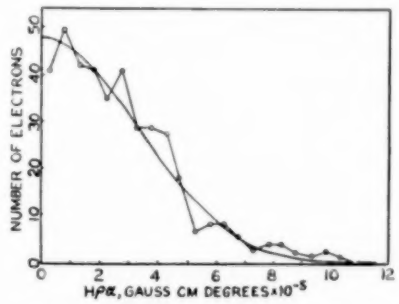

FIG. 6. Scattering of electrons by Pb, 0.157 g/cm².

[11] M. E. Rose, Phys. Rev. **57**, 556A (1940).
[12] H. A. Bethe, M. E. Rose and L. P. Smith, Proc. Am. Phil. Soc. **78**, 573 (1938).
[13] The experimentally observed $\bar{\alpha}$ was used in plotting the Gaussian. There would be a slight broadening of the curve if a theoretical value of $\bar{\alpha}$ were used instead.

TABLE I. *Data on scattering by carbon (0.82 g/cm²).*

NUMBER OF TRACKS	ENERGY INTERVAL MEV	OBSERVED $\bar{\alpha}$	OBSERVED $(H\rho\alpha)_{Av}\cdot10^{-5}$	WILLIAMS $(H\rho\alpha)_{Av}\cdot10^{-5}$	RATIO OF OBSERVED TO WILLIAMS	GOUDSMIT-SAUNDERSON APPROXIMATE $(H\rho\theta)_{Av}\cdot10^{-5}$	RATIO OF OBSERVED TO G-S
302	3–6	12.5°	2.27	2.56	89%	2.51	91%
243	6–8	8.4°	2.12	2.50	85%	2.45	87%
297	9–11	7.0°	2.19	2.49	88%	2.44	90%
842	3–11	9.4°	2.20	2.51	88%	2.46	90%

TABLE II. *Scattering of 6-Mev electrons in various metals.*

FOIL	$\frac{\sigma}{G}$ G/CM^2	NUMBER OF TRACKS	OBSERVED $\bar{\alpha}$	OBSERVED $(H\rho\alpha)_{Av}\cdot10^{-5}$	WILLIAMS $(H\rho\alpha)_{Av}\cdot10^{-5}$	RATIO OF OBSERVED TO WILLIAMS	GOUDSMIT-SAUNDERSON APPROXIMATE $(H\rho\theta)_{Av}\cdot10^{-5}$	RATIO OF OBSERVED TO G-S
Cu	0.174	543	9.0°	1.93	2.20	88%	2.08	93%
Fe	0.173	435	9.2°	1.84	2.11	87%	1.98	93%
Cd	0.111	633	9.4°	2.01	2.13	94%	2.01	100%
Pb	0.072	641	8.6°	1.72	2.07	83%	1.98	87%
Pb	0.157	397	10.3°	2.68	3.21	84%	3.04	88%
Pb	0.362	273	11.4°	4.03	5.12	79%	4.90	82%
PbO	0.076 (0.070 Pb)	635	9.2°	1.76	2.08	85%	2.00	88%
$Pb(ClO_4)_2$ Solution	0.070 Pb	313	8.8°	2.21	2.75	81%	2.62	84%

It should be noted that while most of the scattering materials listed in the tables are polycrystalline solids, two materials were used which were intended to be amorphous, PbO and $Pb(ClO_4)_2$.[14] The purpose of this was to compare the scattering in crystalline and non-crystalline materials under nearly identical conditions. The lead perchlorate solution was considered to be a particularly good approximation to an amorphous scatterer, because there could be little order in the arrangement of the lead atoms in the solution and one could consider the scatterer to be very much like a "lead gas."

CONCLUSIONS

The results seem to indicate that the scattering in carbon and other elements at the lower end of the atomic number scale is somewhat below the theoretically predicted values. These results are in agreement with our previous work on carbon,[15] but diverge considerably from the values reported by Sheppard and Fowler,[16] who found the scattering of 10-Mev electrons to be 114 percent of theory (Williams) for carbon foils of 0.21 g/cm² and 0.61 g/cm².

The experimental values for lead are also appreciably less than the theoretically predicted values, but the agreement with theory appears to be better than obtained by Sheppard and Fowler,[16] who found 55 percent of theory

[14] PbO in an amorphous form (massicot) was prepared in the following manner: lead hydroxide was first obtained by means of the reaction

$$PbCl_2+2NH_4OH\rightarrow Pb(OH)_2+2NH_4Cl.$$

The lead hydroxide was then deposited on filter paper in several layers by forced filtering, care being taken to obtain uniform deposits. Several of these sheets of filter paper were carefully put together while wet and baked in the absence of air from 5 to 6 hours at 200 degrees centigrade. This caused the formation of yellow lead oxide according to the reaction

$$Pb(OH)_2+\text{heat}\rightarrow PbO+H_2O.$$

The resulting foil was used as the scatterer, appropriate corrections being made for the presence of oxygen and the filter paper. Lead perchlorate was prepared in the following manner:

$$PbO+2HClO_4\rightarrow Pb(ClO_4)_2+H_2O.$$

The scatterer consisted of a cell having 0.2-mm glass walls containing a layer of lead perchlorate solution 2 mm thick with a concentration of 0.35 gram per cubic centimeter of lead, thus having a concentration of lead per square centimeter approximately the same as the thinnest lead foil used. The scattering power of all the atoms of the cell (including the glass walls) was taken into account, but was small compared to that of the lead. A preliminary report on the liquid scatterer was given at the Pittsburgh (1940) meeting of the American Physical Society: N. L. Oleson, K. T. Chao and H. R. Crane, Phys. Rev. **58**, 201A (1940).

[15] N. L. Oleson, K. T. Chao, J. Halpern and H. R. Crane, Phys. Rev. **56**, 482, 1171 (1939).

[16] C. W. Sheppard and W. A. Fowler, Phys. Rev. **57**, 283 (1940).

(Williams) for a foil of 0.157 g/cm² and 71 percent for a foil of 0.362 g/cm². The lead perchlorate solution gives approximately the same results as the polycrystalline lead foils.

The best agreement between theory and experiment is obtained for the case of the cadmium scatterer, an element in the middle of the periodic table.

In conclusion, we believe that it is possible to state that there is evidence that the scattering for light and heavy elements is appreciably less than the theoretical values, while the middle elements appear to be in good agreement with theory. Although we have no theoretical proposals to make concerning these discrepancies, it might seem reasonable to expect the best agreement for the middle elements, because here the number of orbital electrons is large enough to justify the use of a statistical treatment of their distribution and also the atomic number is not so large that there is doubt as to the validity of the Born approximation.

Our attempts to detect an effect of crystal structure gave negative results within our rather broad limits of error. This, of course, does not preclude the possibility that a small effect exists.

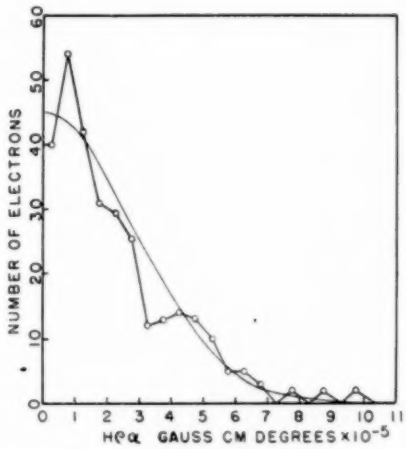

FIG. 7. Scattering of electrons by a solution of lead perchlorate.

We wish to thank Professor Goudsmit for his continued interest and for the opportunity to discuss with him various aspects of the problem. This work was made possible by a grant from the Horace H. Rackham Fund.

SEPTEMBER 1, 1941 PHYSICAL REVIEW VOLUME 60

Theory of the Magnetron. I

LÉON BRILLOUIN
University of Wisconsin, Madison, Wisconsin
(Received June 4, 1941)

A complete calculation of space charge and field repartition is given for a magnetron working under steady conditions. Electrons leaving the filament gradually acquire an angular velocity, and for distances greater than a certain length L, these electrons describe spirals around the filament. This very important length L is defined by

$$L^2 = -eI/m\omega_H^3.$$

I = current per unit of length of the filament, ω_H = Larmor's angular velocity. Under critical conditions, that is, when the magnetic field is just high enough to cut the anodic current I, the electron cloud rotates about the filament almost as a solid body with an angular velocity ω_H. A study of small oscillations with cylindrical symmetry shows that these oscillations have a proper frequency $\sqrt{2}\omega_H$, and that the magnetron is able to yield an internal *negative resistance* for certain frequency bands near $\sqrt{2}\omega_H$; this explains how a magnetron with one cylindrical anode can sustain continuous oscillations in an electric circuit.

1. INTRODUCTION. GENERAL OBSERVATIONS ON THE PART PLAYED BY THE MAGNETIC FIELD—LARMOR'S THEOREM

FOLLOWING Hull's original work on magnetrons, a large number of theories have been formulated; the majority, however, appear inadequate or inexact. Certain authors considered the electronic motion while neglecting the space charge; others used the space charge computed by Langmuir for a diode without a magnetic

field. Such studies necessarily are highly inaccurate, since a powerful magnetic field considerably modifies the electronic paths and, consequently, the space charge. Contrariwise, authors who have endeavored to evaluate the space charge in the presence of a magnetic field do not appear to have provided practicable solutions. It therefore appears necessary to consider the problem afresh and to compute directly both the space charge and the potential distributions in the magnetron; without these essential data, the development of a coherent theory is impossible.

As a preliminary study to the theory of the magnetron it is interesting to state some general results about electronic paths in an electrical field repartition with central symmetry, when a magnetic field is acting on the system. Let us assume an electrical device where the potential $V(r)$ is a function of the distance r to the z axis, while the magnetic field H lies parallel to the same axis. The equations of motion follow:

$$\begin{aligned} m\ddot{x} &= -e\frac{\partial V}{\partial x} + \mu_0 e v_y H = -e\frac{\partial V}{\partial r}\frac{x}{r} + \mu_0 e\dot{y}H, \\ m\ddot{y} &= -e\frac{\partial V}{\partial y} - \mu_0 e v_x H = -e\frac{\partial V}{\partial r}\frac{y}{r} - \mu_0 e\dot{x}H, \end{aligned} \tag{1}$$

where μ_0 is the magnetic permeability in vacuum. By multiplying the first equation by $-y$ and the second by x, adding and integrating, the integral of the moment of momentum is obtained:

$$\mathfrak{J} = m(x\dot{y} - y\dot{x}) + \tfrac{1}{2}\mu_0 eHr^2 = c^{te}. \tag{2}$$

Let us introduce cylindrical coordinates r, θ, z around the z axis

$$\mathfrak{J}/m = r^2\dot{\theta} + \tfrac{1}{2}\mu_0(e/m)Hr^2 = C;$$

hence

$$\dot{\theta} = \omega_H + C/r^2, \tag{3}$$

where

$$\omega_H = -\tfrac{1}{2}\mu_0(e/m)H \tag{4}$$

represents Larmor's angular velocity. To determine the orders of magnitude, if H be measured in gauss while all the equations are written in e.s.c.g.s. units, it is necessary to take:

$$\mu_0 = c^{-2}, \quad H_{\text{e.s.c.g.s.}} = cH_{\text{gauss}},$$

c = velocity of light; on the other hand, $-e/m = +5.3\times10^{17}$ e.s.c.g.s. since e is negative; then

$$\omega_H = 0.884\times10^{7}H_{\text{gauss}}, \tag{5}$$

which, for a field of 500 gauss, gives an angular velocity of 4.42×10^{9}.

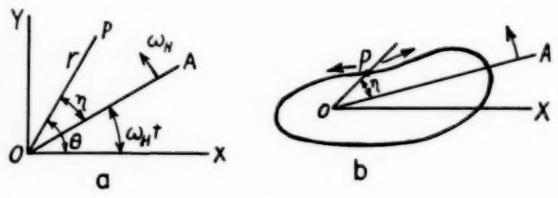

FIG. 1.

If we revert to the equation of electron movement in polar coordinates r and θ, for θ, the simple result of (3) has been derived; for r,

$$m\ddot{r} = -e\frac{\partial V}{\partial r} + \mu_0 eHr\dot{\theta} + mr\dot{\theta}^2, \tag{6}$$

where the electric, Lorentz, and centrifugal forces will be recognized. If we replace $\mu_0 eH$ by the equivalent expression, $-2m\omega_H$, it is found that

$$\ddot{r} = -\frac{e}{m}\frac{\partial V}{\partial r} - 2\omega_H\dot{\theta}r + r\dot{\theta}^2, \tag{7}$$

a result which may be expressed in this way:

$$\frac{\ddot{r}}{r} = -\frac{e}{mr}\frac{\partial V}{\partial r} + (\dot{\theta} - \omega_H)^2 - \omega_H^2. \tag{8}$$

Comparing Eqs. (3) and (8) we notice that the angular velocity comes in both formulae with the difference $\dot{\theta} - \omega_H$ which justifies the following treatment: In the xy plane, let us use a rotating axis OA, the angular velocity of which will be equal to ω_H; then the angle η between OP and OA as shown in Fig. 1(a) is

$$\begin{aligned} \eta &= \theta - \omega_H t, \\ \dot{\eta} &= \dot{\theta} - \omega_H, \end{aligned} \tag{9}$$

and Eqs. (3) and (8) yield

$$\dot{\eta} = \frac{C}{r^2}, \quad \frac{\ddot{r}}{r} = -\frac{e}{mr}\frac{\partial V}{\partial r} + \dot{\eta}^2 - \omega_H^2. \tag{10}$$

The second equation contains only $\dot{\eta}^2$, which means that two opposite values, $\pm C$, giving opposite angular velocities $\pm\dot{\eta}$ for each value of r

will yield similar orbits in the r, η plane. The general solution is then represented by one orbit, rotated around the center O, Fig. 1(b), with Larmor's precession ω_H, and by allowing the electron to run on this orbit (in the rotating r, η plane) with opposite velocity. This is the most general statement for Larmor's theorem. The usual case considered in atomic structures refers to problems in which the angular velocity $\dot{\eta}$ on the orbit is very much greater than Larmor's ω_H, so that the ω_H^2 term in Eq. (10) can be neglected; the rotating orbits are then similar to the unperturbed orbit obtained when the magnetic field is zero.

In the problems connected with the theory of the magnetron, such an approximation will not be allowed, and it will prove necessary to take care of the ω_H^2 term. Let us, for instance, suppose that we want to study the motions of electrons inside of a cloud of constant density, ρ. The potential distribution V is given by

$$\Delta V=-\frac{1}{r}\frac{\partial}{\partial r}\left(r\frac{\partial V}{\partial r}\right)=-4\pi\rho \text{ e.s.c.g.s.}, \quad (11)$$

$$V=-\pi\rho r^2,$$

where V and $\partial V/\partial r$ are zero for $r=0$. Equations (10) yield

$$\dot{\eta}=C/r^2, \quad \ddot{r}/r=(e/m)2\pi\rho+\dot{\eta}^2-\omega_H^2. \quad (12)$$

The first condition gives the angular velocity as a function of r on *each orbit*, but different orbits in the cloud may correspond to different values of C, according to the initial velocity distributions for each special problem.

For instance, we may suppose circular orbits, each of them corresponding to a certain C value. Such circular orbits will keep the electronic density ρ of the cloud constant; $\ddot{r}$ being zero, the angular velocity is given by

$$\dot{\eta}=\pm\left(\omega_H^2-\frac{e}{m}2\pi\rho\right)^{\frac{1}{2}},$$

$$\dot{\theta}=\omega_H+\dot{\eta}=\omega_H\pm\left(\omega_H^2-\frac{e}{m}2\pi\rho\right)^{\frac{1}{2}}. \quad (13)$$

In each of the two $\pm$ solutions the angular velocity is constant, independent of r, and the electronic cloud is rotating as a solid body around the Oz axis.

A constant linear velocity along the z axis may be added without any change in the preceding solutions, thus giving a possible type of electronic motions in the form of "magneto-cathodic rays."

At the limit $\rho=0$ one finds the well-known result that free electrons in a magnetic field may either stay at rest ($\dot{\theta}=0$, sign $-$) or describe circular orbits with an angular velocity twice the Larmor rotation ($\dot{\theta}=2\omega_H$, sign $+$).

Stable electronic clouds in magnetic fields are possible when their density ρ is smaller than a certain maximum value

$$0\leqslant\rho\leqslant\rho_m, \quad \rho_m=(m/2\pi e)\omega_H^2. \quad (14)$$

If a cloud of higher uniform density had been artificially created, it would expand according to Eq. (12) ($\ddot{r}>0$), until it reached the limit ρ_m. Clouds of density smaller than ρ_m may be stable or expand or contract to the limit ρ_m, the type of solution depending on the initial conditions of the cloud.

It will be found that electronic clouds of such types play a very important role in the theory of the magnetron.

2. Cylindrical Magnetron—Static Case

The magnetron is assumed to consist of a filament of radius a and a cylindrical anode of radius b, the magnetic field H accurately paralleling the filament (axis Oz). It is assumed that electrons without appreciable speed are emitted from the filament, and that the electric field on the filament is zero, provided the anode current is below saturation; hypotheses which have both been generally accepted since they were formulated by Langmuir. Distribution of the cylindrical space charge can thus be obtained; the potential V is solely a function of r. The equations of motion are Eqs. (1), (2), (3), and (4) of the preceding section.

The static case, which will first be considered, is characterized by the fact that V does not depend on time.

The constant C of (3) is determined by the fact that electrons are emitted without speed from the filament, so that $\dot{\theta}$ is zero for $r=a$:

$$\dot{\theta}=\omega_H(1-a^2/r^2). \quad (15)$$

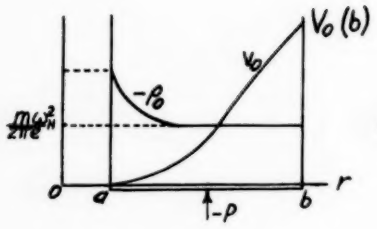

FIG. 2. Critical conditions, $I=0$.

The Lorentz force, due to the magnetic field H, does not influence the velocity since it is perpendicular to the latter. Energy conservation accordingly may be written:

$$\tfrac{1}{2}mv^2+eV=\tfrac{1}{2}m(\dot r^2+r^2\dot\theta^2)+eV=C'$$

and this new constant is zero if

$$V(a)=0 \text{ on the filament;} \qquad (16)$$

hence

$$\dot r^2+\omega_H^2r^2(1-a^2/r^2)^2+(2e/m)V=0. \qquad (17)$$

The equations of movement, therefore, may be integrated directly from (15) and (17) without determining the potential distribution as a function of r.

In (17) one result is at once evident: since the velocity of rotation $\dot\theta$ is determined by the magnetic field, the kinetic energy at the distance r cannot be less than:

$$\frac{m}{2}r^2\dot\theta^2=\frac{m}{2}\omega_H^2r^2\left(1-\frac{a^2}{r^2}\right)^2.$$

Hence, if the potential $V(r)$ does not suffice to give the electron greater kinetic energy, the radial velocity $\dot r$ is annulled and the current is interrupted. Consequently

$$\dot r=0, \quad -(2e/m)V_0=\omega_H^2r^2(1-a^2/r^2)^2. \qquad (18)$$

This is Hull's *limiting value of the potential* V_0 at the distance r, where the anode current is just cut off by the magnetic field. This limiting value $V_0(r)$ is thus defined without the necessity of determining the distribution of the space charge or the potentials between the anode and cathode —a remarkable fact which discloses the possibility of finding the correct value of the critical potential $V_0(r)$ without considering the space charge.

Let us now come back to Eq. (7) in polar coordinates. Making use of Eq. (15) we find

$$\begin{aligned} m\ddot r &= -e\partial V/\partial r-mr\dot\theta(2\omega_H-\dot\theta)\\ &= -e\partial V/\partial r-m\omega_H^2r(1-a^4/r^4)\\ &= -(\partial/\partial r)[eV+\tfrac{1}{2}m\omega_H^2(r^2+a^4/r^2)]. \end{aligned} \qquad (19)$$

The radial acceleration $\ddot r$ is accordingly governed by an apparent potential function $P(r)$:

$$\begin{aligned} &m\ddot r=-e(\partial P/\partial r),\\ &P=V-V_0=V+(m/2e)\omega_H^2(r-a^2/r)^2. \end{aligned} \qquad (20)$$

In the function $P(r)$ a constant $-m\omega_H^2a^2$ has been added in order to reduce $P(a)$ to zero on the filament $r=a$; thus the same function is made to appear as in the energy equation (17). A fact worthy of emphasis is the following:

With the apparent potential $P(r)$, the radial movement of the electron may be studied by means of Eq. (20) without considering the rotation ω around the filament. These general results are valid in all cases either with or without space charge.

3. Static Space Charge: Critical Potential

To obtain a potential distribution in a static state, it is necessary to introduce the space charge $\rho(r)$, a function of the radius r and independent of time. From the cylindrical symmetry of the system we have:

$$\Delta V=\frac{1}{r}\frac{\partial}{\partial r}\left(r\frac{\partial V}{\partial r}\right)=-4\pi\rho, \quad I=2\pi r\rho v_r. \qquad (21)$$

The current I, per unit length of filament, is a constant independent of r; v_r is taken from (17) and the following is obtained:

$$\begin{aligned} \frac{\partial}{\partial r}\left(r\frac{\partial V}{\partial r}\right)&=-\frac{2I}{v_r}\\ &=-\frac{2I}{\left[-\dfrac{2e}{m}V-\omega_H^2\left(r-\dfrac{a^2}{r}\right)^2\right]^{\frac{1}{2}}}. \end{aligned} \qquad (22)$$

The conditions are the following:

$$V(a)=0 \text{ on the filament.}$$

$$(\partial V/\partial r)_{r=a}=0 \text{ no saturation.}$$

Since the non-linear Eq. (22) would require detailed discussion, it is preferable to start with

the simpler cases where *the current I is zero*. Two methods are available, according to Eq. (21):

$$\text{(A)} \qquad \rho \neq 0, \quad v_r = 0,$$

which yields

$$V_0(r) = -\frac{m}{2e}\omega_H^2\left(r - \frac{a^2}{r}\right)^2, \quad P(r) = 0. \quad (23)$$

Expression (23) completely satisfies the two limiting conditions of (22).

$$\text{(B)} \qquad \rho = 0, \quad v_r \neq 0;$$

hence,

$$V = B \log r + C, \quad (24)$$

which corresponds to a definitely electrostatic potential without space charge.

Let us now examine the distributions of the charges and potential in a magnetron when the potential of the anode ($r=b$) is rather low so that no current flows.

The limiting case corresponding to the maximum possible potential on the plate, with no current flowing, is obtained by taking

$$V_0(b) = -(m/2e)\omega_H^2(b - a^2/b)^2 \quad (18)$$

as shown in preceding section, Eq. (18); *it is the critical potential*. The density is not zero, and space charges are present throughout the medium between the filament and anode; Eq. (21) gives their value:

$$\rho_0(r) = (m\omega_H^2/2\pi e)(1 + a^4/r^4). \quad (25)$$

The radial velocity is zero throughout; the electrons follow circular trajectories, centered on the filament. The Lorentz and centrifugal forces are in exact equilibrium with the electrostatic force in Eq. (19), as is also evident from (20), since the distribution (18), (25) completely annuls $P(r)$.

In the case of a potential $V_0(b)$ below the critical potential, there is obtained a charge distribution (25) extending from the filament ($r=a$) up to a certain cylinder $r=b'$. This particular form of distribution then stops abruptly; the potential distribution continues in the form of a logarithmic field at the cylinder b', and the two constants B and C may be determined by the conditions:

$$-\frac{m}{2e}\omega_H^2\left(b' - \frac{a^2}{b'}\right)^2 = B \log b' + C$$

$$-\frac{m}{e}\omega_H^2\left(b' - \frac{a^4}{b'^3}\right) = \frac{B}{b'}. \quad (26)$$

When the potential $V(b)$ of the anode is progressively lowered, the space charge is correspondingly restricted to a decreasing cylinder b' around the filament; and, when $V(b)$ is zero, the space charge disappears.

Figure 2 illustrates the case of critical potential $V_0(b)$; the different curves represent the space charge density ρ, the electrostatic potential $V(r)$ and the apparent radial potential $P(r)$.

Figure 3 shows the potential distribution, $V(r)$, for anode potentials lower than the critical value. The apparent potential energy of the electron is eP or $-\epsilon P$, ϵ designating the absolute value of an electron charge. Hence,

$$P = V - V_0$$

according to (20). The behavior of this function is easily described and is important to recognize inasmuch as the apparent energy P governs the electronic radial movements.

In the critical state (Fig. 2), $-P$ is identically zero. The electrons of the cloud forming the space charge have no radial velocity.

When the magnetron is below its critical state (Fig. 3), the apparent potential $-P$ rises between b' and b in front of the anode. The critical distribution shown in Fig. 1 seems to be that described by Hull[1] in a brief note, for which he claims to have found good experimental evidence from space charge density measurements.

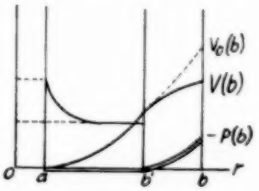

FIG. 3. Potential distribution, $V(r)$ for anode potentials lower than the critical value.

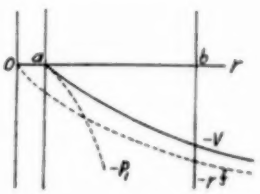

FIG. 4. Values from Langmuir's solution for the diode.

[1] A. W. Hull, Phys. Rev. **23**, 112A (1924).

4. Direct-Current Condition without Saturation

Since the fundamental equation (22) has just been considered for the various cases where the current is nil, it is now desirable to determine the direct-current conditions. Equation (22) will be transcribed, with the unknown function taken as the apparent potential $P(r)$ defined in (20) instead of the electrostatic potential $V(r)$.

$$\frac{\partial}{\partial r}\left(r\frac{\partial V}{\partial r}\right)=\frac{\partial}{\partial r}r\frac{\partial}{\partial r}(P+V_0)=-I\left(-\frac{2m}{e}\right)^{\frac{1}{2}}\frac{1}{P^{\frac{1}{2}}}.$$

If we replace V_0 by its value (20) we have

$$P^{\frac{1}{2}}\left[-\frac{2m\omega_H{}^2}{e}\left(r+\frac{a^4}{r^3}\right)+\frac{\partial}{\partial r}r\frac{\partial P}{\partial r}\right]=-I\left(-\frac{2m}{e}\right)^{\frac{1}{2}}. \quad (27)$$

This equation is rigorous. The solution $P(r)$ must be such that conditions (22) will be satisfied on the filament.

$$P(a)=0, \quad \partial P/\partial r=0, \quad r=a$$

on the filament (27).

The solution of (27) can only be derived approximately; two distinct regions must be considered as limiting cases:

A. Proximity to filament

The second member remains constant and, on the filament, P is nil; the term in brackets must, therefore, be infinite. The required solution is of the type:

$$P=A(r-a)^n,$$

which gives

$$A^{\frac{1}{2}}(r-a)^{n/2}\left[-\frac{2m\omega_H{}^2}{e}2a+nA(r-a)^{n-1}+aAn(n-1)(r-a)^{n-2}\right]=-I\left(-\frac{2m}{e}\right)^{\frac{1}{2}}.$$

If we take $n=4/3$, the two first terms are zero; in view of the factor $(r-a)^{n/2}$ the last term remains finite and it is found that:

$$P=\tfrac{1}{2}\left(-\frac{m}{e}\right)^{\frac{1}{2}}\left(\frac{9I}{a}(r-a)^2\right)^{\frac{2}{3}} \quad r-a\ll 1. \quad (28)$$

This solution is valid only in the immediate vicinity of the cathode, while $r-a$ remains very small. At increasing distances from the cathode, account must be taken of the fact that $\partial P/\partial r$ is no longer zero; and the magnetic term in ω_H must be dealt with. Let us first determine what happens at a short distance from the filament where the magnetic term still remains very small; the problem of the ordinary diode is re-encountered.

The diode without a magnetic field has been dealt with by Langmuir;[2] the potentials V and P are identical and Eq. (27) reduces to

$$P^{\frac{1}{2}}\frac{\partial}{\partial r}r\frac{\partial P}{\partial r}=-I\left(-\frac{2m}{e}\right)^{\frac{1}{2}}. \quad (29)$$

For $r\gg a$, far from the filament, a solution is found in $r^{\frac{4}{3}}$ and the complete solution may be written:

$$P_L=\tfrac{1}{2}(-m/e)^{\frac{1}{2}}(9I\beta^2 r)^{\frac{2}{3}}, \quad (30)$$

where β^2 is a function of r/a, calculated by Langmuir:

r/a	1	1.25	1.5	1.75	2	2.5	3
β^2	0	0.045	0.116	0.2	0.275	0.405	0.512

4	5	6	7	8	9	10	15	∞
0.665	0.775	0.818	0.867	0.902	0.925	0.94	0.978	1

Equation (30) presents the same structure as (28) and correspondence is thus established in the vicinity of the filament. The potential P is obtained by replacing $\beta^2 r$ by $(r-a)^2/a$. With r close to a:

$$\beta^2\approx(r-a)^2/ar. \quad (31)$$

Comparison with (30) shows that this approximation is valid only up to $r=1.25a$; that is, in the immediate vicinity of the filament. This indication gives the limit of validity of (28), which should be replaced by Langmuir's Eq. (30) when distances beyond the immediate vicinity of the cathode are involved.

Figure 4 shows the shapes of the various curves.

---

[2] I. Langmuir, Phys. Rev. **2**, 458 (1913). An approximate solution may be found:

$$P=\tfrac{1}{2}(9I)^{2/3}\left(-\frac{m}{e}\right)^{1/2}\frac{(r-a)^{4/3}}{r^{2/3}}$$

it yields correct results for very small or very large r, the error is about 20 percent near $r=4a$.

B. Distant from filament

At a considerable distance from the filament the Langmuir equation gives low values for the term $(\partial/\partial r)[r(\partial P/\partial r)]$. Contrariwise, the magnetic term within the brackets of (27) increases indefinitely. A moment therefore arrives when this first term becomes preponderant. At the limit, the second term may be neglected and the first term kept. An asymptotic solution P_ω, valid at a great distance, is:

$$r \gg a,$$

$$P_\omega(r) = -I^2 \frac{e}{2m\omega_H{}^4}\left(r+\frac{a^4}{r^3}\right)^{-2} \approx -I^2 \frac{e}{2m\omega_H{}^4 r^2}. \quad (32)$$

It is now necessary to discuss how to join these two extreme cases with a view to ascertaining the corresponding values of r and the form of function $P(r)$ obtained.

By comparing the equations, an expression $-eI/m\omega_H{}^3$ appears, homogeneous to a certain length L squared. The following gives an indication of the order of magnitude:

$-e/m = 5.3\times10^{17}$ (e.s.c.g.s.),
$I = 3\times10^6 J$ (J in milliamperes; I in e.s.c.g.s. units).

If we calculate ω_H according to (5) and express H in gauss:

$$L^2 = -eI/m\omega_H{}^3 = 2.3\times10^3 J/H^3. \quad (33)$$

The role played by the characteristic length L is very important and has now to be discussed.

First, the condition stated at the beginning of Section 3 must be satisfied in order to justify use of the solution (32); this necessitates:

$$\frac{\partial}{\partial r}\left(r\frac{\partial P_\omega}{\partial r}\right) = -\frac{2I^2 e}{m\omega_H{}^4 r^3} \ll -\frac{2m}{e}\omega_H{}^2 r.$$

By neglecting a, this condition reduces to

$$r \gg L.$$

For weak fields, which scarcely disturb the diode, the length L is much greater than the dimensions of the bulb; if the field increases, however, the length L decreases considerably to the order of magnitude of the interior dimension of the bulb and may even drop to very low values;

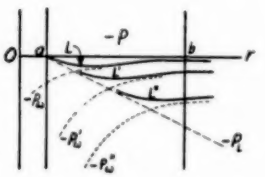

FIG. 5. Value of the apparent potential P_ω for various values of L.

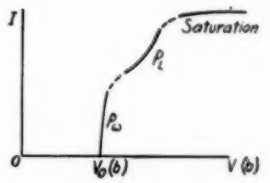

FIG. 6. Magnetron characteristic.

for some hundreds of gauss, L is of the order of some tenths of a mm.

The length L then gives the magnitude of the distance where the Langmuir solution P_L (always valid in the immediate vicinity of the filament) has to rejoin with the solution P_ω which is valid at a great distance.

As a rough criterion of the distance of coincidence, we take the condition:

$$P_L(r) = P_\omega(r),$$

then

$$\tfrac{1}{2}(9I\beta^2 r)^{\frac{1}{3}}(-m/e)^{\frac{1}{3}} = -I^2 e/2m\omega_H{}^4 r^2; \quad (34)$$

hence

$$9\beta^2 r^4 = L^4.$$

The curve representing the apparent potential $P(r)$ is consequently known by the expressions P_L (for $r \ll L$) and P_ω (for $r \gg L$); it can, in any case, be plotted approximately. Figure 5 shows curves for various values of L between the cathode ($r=a$) and the anode ($r=b$).

If the anode radius b is appreciably greater than the length L, the formula $P_\omega(R)$ of (32) gives the anode voltage, calculated from the critical voltage $V_0(R)$; if, however, the length L is very great, the magnetic field being weak, Langmuir's curve P_L is used. Figure 6, accordingly, shows the magnetron characteristic; the internal resistance R is zero in the vicinity of the critical point.

Reverting to the curves of Fig. 5, it should be noted that the electrons, after leaving the filament ($r=a$), first reach the Langmuir region and then travel toward $r=L$ through a region of low apparent potential energy, thereafter rebounding (approaching the anode) toward higher potential energies only slightly below the potential energy of the cathode. The expression $-P(r)$ represents, but for the factor $\epsilon = |e|$, the apparent potential energy of the electrons, controlling their radial

movements (Eq. (20)). The speed of rotation around the filament is defined by (15). The curves $-P(r)$ show that the electrons are accelerated from a to L and retarded from L to b. The space charge thus is increased in the second region; close to the filament, Langmuir's space charge applies, and, at a great distance, the constant space charge of (25) applies approximately

$$r \gg L, \quad \rho \approx m\omega_H^2/2\pi e. \tag{35}$$

This space charge density far away from the filament is just the density we have found in Eq. (14) as being the greatest possible density of electrons in a given magnetic field. A more detailed study would require calculation of the junction of the curves in the region L. The following, however, is pertinent:

The electronic paths start radially from the filament; they are slightly curved in the region $r=L$ and then turn around the filament for $r \gg L$, as shown in Fig. 7. This can be understood readily from the following considerations: Let V_r and V_θ be the radial and rotational components of electronic velocity; Eqs. (15) and (21) yield:

$$\frac{V_\theta}{V_r} = \frac{r\dot{\theta}}{I} 2\pi r\rho = \frac{2\pi r^2 \rho}{I} \omega_H \left(1 - \frac{a^2}{r^2}\right).$$

Instead of computing the ratio V_θ/V_r, let us calculate

$$\frac{\rho V_r}{\rho_0 V_\theta} = \frac{2\pi r^2 \rho_0}{I} = \frac{r^2 m \omega_H^3}{eI}\left(1 - \frac{a^2}{r^2}\right)\left(1 + \frac{a^4}{r^4}\right), \tag{36}$$

where ρ_0 is the space charge density (25) in the region $r \gg L$. If the radius a of the cathode is neglected, as a first approximation, it is seen that the ratio $\rho V_r/\rho_0 V_\theta$ equals -1 when $r=L$, which proves that V_r and V_θ are of the same order of magnitude at a distance L from the filament. It appears from this discussion that the junction between the two asymptotic solutions A (near the filament) and B (far away from it) has to take place about the distance L from the filament. Series of approximations starting from both sides can be obtained and have already been published in a former paper.[3]

[3] L. Brillouin, "Theory of the magnetron," Elec. Commun. **20**, No. 1 (1941).

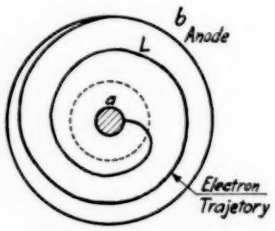

FIG. 7. Electronic paths from filament to anode.

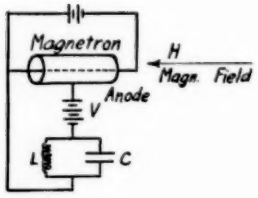

FIG. 8. Oscillator circuit.

5. Oscillations in a Magnetron with Cylindrical Anode: Some General Remarks

Different types of magnetrons are practically used for generating electromagnetic oscillations; some of them possess one anode, of cylindrical shape. Oscillations of large amplitude are often obtained from these devices, but large oscillations are rather difficult to discuss theoretically and the calculations will be given only for the case of small oscillations, which do not introduce too great a perturbation in the original charge density distribution.

The theoretical discussion will be conducted with the following approximations: The formula giving the electric current has to be completed with an additional term, taking account of Maxwell's displacement current. In more general problems, one should also take account of the magnetic fields induced by the current flowing inside the magnetron, but we shall assume the cylindrical symmetry to be obeyed for all quantities, in which case there is no induced magnetic field for a magnetron of infinite length. Magnetic fields would appear only outside of a magnetron of finite length and result in radiation of electromagnetic waves from the magnetron. This is, of course, a very small and secondary effect, causing some damping to the oscillations in the magnetron.

Equations of Sections 1 and 2 will thus be modified in the following way: The charge density ρ and the radial electric field E will be considered as functions of r and t, an assumption which secures cylindrical symmetry at any time. Equation (11) becomes

$$\frac{1}{r}\frac{\partial}{\partial r}(rE) = 4\pi\rho, \quad E = -\frac{\partial V}{\partial r}. \tag{37}$$

The current I, including displacement current, will be written

$$I=2\pi r\left(\rho v_r+\frac{1}{4\pi}\frac{\partial E}{\partial t}\right)=2\pi\rho r\dot{r}+\frac{r}{2}\frac{\partial E}{\partial t}. \quad (38)$$

The dielectric constant ϵ_0 in vacuum, has been taken 1 in e.s.c.g.s. units. As is well known from general proofs, introduction of the displacement term secures the constancy of I along the whole circuit, which means here that I is independent of the distance r, and a function only of t. All other formulae from Section 2 still apply, and especially Eqs. (15), (19), and (20). Time derivatives may be taken either at a given place, or following the motion of an electron; these two definitions will be distinguished this way:

$$\begin{cases} \partial/\partial t & \text{derivative at } r \text{ constant or ordinary partial derivative,} \\ d/dt=\partial/\partial t+v_r\partial/\partial r & \text{following the motion of an electron moving with the velocity } v_r,\ v_\theta. \end{cases} \quad (39)$$

All quantities being independent of θ, because of cylindrical symmetry, a term in $v_\theta\partial/\partial\theta$ has been omitted in formula (39). Equation of motion (20), for instance, has to be written

$$d^2r/dt^2=-e\partial P/\partial r. \quad (40)$$

A well-known integration method, which has proved very useful in most electronic problems, was omitted on purpose in the preceding sections for the reason that it leads to some difficulties which will be discussed now. The method consists in taking the derivative d/dt of the product rE, following the motion of an electron:

$$\frac{d}{dt}(rE)=\frac{\partial}{\partial t}(rE)+\dot{r}\frac{\partial}{\partial r}(rE)$$

$$=r\frac{\partial E}{\partial t}+\dot{r}4\pi\rho r=2I \quad (41)$$

and in using Eqs. (37) and (38). As noticed before, $I(t)$ is independent of r, which allows easy integration:

$$rE(r,t)=2\int_{t_0}^{t}I(t)dt. \quad (42)$$

t_0 is the time at which one given electron has left the filament, and t the instant when it reaches the distance r.

Let us now show the difficulties involved in the use of this formula, by applying it to the static case. E is independent of t; hence

$$E(r)=2I\tau/r, \quad (43)$$

where $\tau=t-t_0$ is the transit time for an electron going from the filament to the distance r. Suppose the magnetic field to be such as to cut the anodic current, according to condition (18); I is naught, but electrons in this case are moving in circular orbits about the filament, with no radial velocity at all; hence the transit time τ is infinite, while E keeps a finite value. Many theoreticians attempting to use (43) without a former knowledge of the solution were led to entirely wrong conclusions.

6. Small Oscillations in a Magnetron with Cylindrical Anode

After the magnetron has been studied in its static condition, without oscillations, all we need do now is to superimpose small oscillations on the static quantities. The amplitude of the oscillations will be specified by a factor ϵ; static continuous quantities are characterized by a subscript c, while alternating quantities will be given a subscript a.

$$\begin{cases} V=V_c(r)+\epsilon V_a(r,t) & \text{electric potential,} \\ I=I_c+\epsilon I_a(t) & \text{electric current independent of } r, \\ r=r_c(t)+\epsilon r_a(t) & \text{position of the electron at the time } t. \end{cases} \quad (44)$$

Because of the supposed smallness of ϵ, all terms in ϵ^2, $\epsilon^3\cdots$ will be neglected. Let us now rewrite the most important formulae, starting with (20):

$$\frac{d^2r_c}{dt^2}+\epsilon\frac{d^2r_a}{dt^2}=\frac{e}{m}\left(\frac{\partial V_0}{\partial r}-\frac{\partial V_c}{\partial r}\right)-\epsilon\frac{e}{m}\frac{\partial V_a}{\partial r}. \quad (45)$$

Potentials V_0 and V_c have to be taken at the point $r_c+\epsilon r_a$ where the electron is located; hence the expansion $V_c(r)=V_c(r_c)+\epsilon r_a[\partial V_c(r_c)/\partial r]$. Constant terms and oscillating terms are easily

separated, and yield the following relations:

$$\frac{d^2r_c}{d.^2}=\frac{e}{m}\left(\frac{\partial V_0(r_c)}{\partial r}-\frac{\partial V_c(r_c)}{\partial r}\right), \tag{46}$$

$$\frac{d^2r_a}{dt^2}=\frac{e}{m}r_a\left(\frac{\partial^2 V_0}{\partial r^2}-\frac{\partial^2 V_c}{\partial r^2}\right)-\frac{e}{m}\frac{\partial V_a}{\partial r}. \tag{47}$$

Treating Eq. (42) in the same way, one gets

$$rE=(r_c+\epsilon r_a)\left(-\frac{\partial V_c}{\partial r}-\epsilon r_a\frac{\partial^2 V_c}{\partial r^2}-\epsilon\frac{\partial V_a}{\partial r}\right)$$

$$=2\int_{t_0}^{t}(I_c+\epsilon I_a)dt;$$

hence two relations are derived

$$r_c\frac{\partial V_c}{\partial r}=-2I_c(t-t_0), \tag{43}$$

$$r_a\frac{\partial V_c}{\partial r}+r_cr_a\frac{\partial^2 V_c}{\partial r^2}+r_c\frac{\partial V_a}{\partial r}=-2\int_{t_0}^{t}I_a dt. \tag{48}$$

Equations (46) and (43) between static quantities have already been obtained in the preceding sections and bring nothing new; this is the result of our hypothesis of infinitely small oscillations. If oscillations of greater amplitude should be considered, terms in ϵ^2, $\epsilon^3\cdots$ could not be neglected any more, and would appear in the static formulae (corresponding to detection phenomena) thus perturbing the static regimen.

Equations (47) and (48) rule the magnetronic oscillations and are linear with respect to the unknown quantities r_a and V_a. Eliminating V_a one easily gets

$$\frac{d^2r_a}{dt^2}-\frac{e}{m}r_a\left[\frac{\partial^2 V_0}{\partial r^2}+\frac{1}{r_c}\frac{\partial V_c}{\partial r}\right]=\frac{2e}{mr_c}\int_{t_0}^{t}I_a dt, \tag{49}$$

where V_0 and V_c result from the study of the static case.

In order to know how the magnetron is able to react on the oscillating circuit connected to it, we need to calculate the internal impedance of the magnetron; we thus want to find the relation between the alternating current $I_a(t)$ flowing through the magnetron, and the alternating potential V_a on its anode. Let us suppose $I_a(t)$ to be given, then Eq. (49) is a linear differential equation with a right-hand term. As is the rule for such equations, we have to study first the linear differential equation without the second member; it is of the ordinary oscillating type, and indicates a proper frequency $\omega(r)$ as a function of r.

$$\omega^2(r)=-\frac{e}{m}\left(\frac{\partial^2 V_0}{\partial r^2}+\frac{1}{r}\frac{\partial V_c}{\partial r}\right). \tag{50}$$

Let us study first the order of magnitudes of these internal proper frequencies. In a magnetron on critical conditions, the potential repartition is given by Eq. (23)

$$V_0=V_c=-(m/2e)\omega_H^2(r-a^2/r)^2; \tag{51}$$

hence

$$\omega^2(r)=2\omega_H^2(1+a^4/r^4),\quad \omega(r)\approx\sqrt{2}\omega_H. \tag{52}$$

Such critical conditions, however, correspond to no anodic current ($I_c=0$) and infinite transit time τ, and cannot be used for sustaining oscillations. We may, however, suppose the magnetron to be very near this critical state, the continuous current I_c keeping a small value, so that the average potential $V_c(r)$ will differ only slightly from $V_0(r)$. The proper frequencies $\omega(r)$ will then keep values very near $\sqrt{2}\omega_H$.

Returning to Eq. (49) we notice its similarity to the equation of a harmonic oscillator acted upon by an external force represented by the right-hand term. A remarkable feature is that this equation contains no damping term, but this is only the result of the initial assumptions outlined in Section 5. A complete theory, including magnetic oscillating fields, should yield equations with a damping term due to outside radiation, as is immediately realized for physical reasons.

We are thus allowed to proceed as though such a damping were actually found in the equations, and search only for the forced oscillations, neglecting free oscillations [solutions of Eq. (49) without right-hand term]. Let us thus suppose conditions very near the critical state and call

$$\tau(r)=t-t_0 \tag{53}$$

the transit time for an electron running from the filament ($r=a$) to the distance r. Supposing

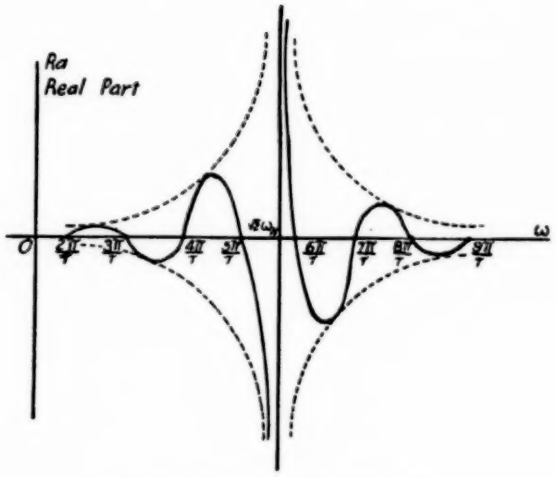

FIG. 9. Approximate values of R_a.

sinusoidal oscillations, we write down

$$I_a = J_a e^{i\omega t}, \quad J_a > 0 \text{ real},$$

$$\int_{t_0}^{t} I_a dt = \frac{J_a}{i\omega}(e^{i\omega t} - e^{i\omega t_0}) = 2\frac{J_a}{\omega}\sin\frac{\omega\tau}{2}e^{i\omega t + i\varphi}. \quad (54)$$

$$\varphi = -\omega\tau/2.$$

Equation (49) takes the following form and defines, for each distance r_c, the amplitude r_a of electronic oscillations.

$$r_a(\omega^2(r) - \omega^2) = \frac{4eJ_a}{mr_c\omega}\sin\frac{\omega\tau}{2}e^{i\omega t + i\varphi}. \quad (55)$$

Phase φ of these oscillations is directly related to the transit time τ.

From the r_a values, one easily calculates V_a using Eq. (47).

$$\frac{\partial V_a}{\partial r} = r_a\left[\frac{\partial^2 V_0}{\partial r^2} - \frac{\partial^2 V_c}{\partial r^2} + \frac{m}{e}\omega^2\right]. \quad (56)$$

V_0 and V_c are very nearly equal to each other (almost critical state) and formula (56) approximately yields

$$\frac{\partial V_a}{\partial r} \approx \frac{m}{e}\omega^2 r_a \approx \frac{4J_a\omega}{r[\omega^2(r) - \omega^2]}\sin\frac{\omega\tau}{2}e^{i\omega t + i\varphi}, \quad (57)$$

$$V_a \approx \frac{4J_a\omega}{\omega^2(r) - \omega^2}\left[\frac{1}{a^2} - \frac{1}{r^2}\right]\sin\frac{\omega\tau}{2}e^{i\omega t + i\varphi}. \quad (58)$$

One must, of course, suppose V_a to be zero on the filament $r = a$. These simpler formulae result from the assumption of a magnetron working very near its critical point. On a more general case, formulae would be of a more complicated type, but one very important point would remain unchanged, namely, the relation between phase angle φ and transit time τ.

Having obtained expressions for alternating current J_a and potential V_a, one immediately finds the internal impedance of the magnetron

$$R_a = \frac{V_a}{J_a} \approx \frac{4\omega}{\omega^2(r) - \omega^2}\left(\frac{1}{a^2} - \frac{1}{r^2}\right)\sin\frac{\omega\tau}{2}e^{-i\omega\tau/2}, \quad (59)$$

$$\varphi = -\omega\tau/2.$$

The question is now to discuss this expression and to see under which conditions it may yield a negative real part, indicating a negative resistance term in the magnetron. It is well known that, in order to be able to sustain oscillations in an electric circuit with positive resistance, an electronic tube must play the role of a negative resistance. Depending on secondary effects in the electronic tube, one may connect this negative resistance in series with the electric circuit or in parallel with it. Magnetrons are actually used with the parallel connection, according to Fig. 8.

7. The Magnetron as a Source of Electrical Oscillations

Referring to formula (59) we notice, first, that the denominator is zero for ω^2 equal to $\omega^2(r)$, which seems to indicate the possibility of infinite internal impedance R_a. This, of course, is the result of some simplifying assumptions discussed in Section 5. A complete theory would include direct radiation from the moving electrons, thus giving a damping term s in the equation, and the impedance R_a would have a denominator avoiding infinity like

$$\{[\omega^2(r) - \omega^2]^2 + s^2\}^{\frac{1}{2}}.$$

At any rate, large values of R_a will only be obtained for

$$\omega \approx \omega(r) \approx \sqrt{2}\omega_H. \quad (60)$$

Now we determine the real part of R_a

$$\mathrm{Re}(R_a)=\frac{2\omega}{\omega^2(r)-\omega^2}\left(\frac{1}{a^2}-\frac{1}{r^2}\right)\sin\omega\tau. \quad (61)$$

Figure 9 gives an approximative visualization of such a function. This will be negative in the following cases:

$$\begin{aligned}&\omega^2<\omega^2(r), \quad \sin\omega\tau<0,\\ &\pi<\omega\tau<2\pi,\\ &3\pi<\omega\tau<4\pi, \quad \cdots\end{aligned} \quad (62)$$

and

$$\begin{aligned}&\omega^2>\omega^2(r), \quad \sin\omega\tau>0,\\ &0<\omega\tau<\pi,\\ &2\pi<\omega\tau<3\pi, \quad \cdots.\end{aligned} \quad (63)$$

We recall that transit time τ in a magnetron may reach values much greater than the period of oscillations; the best values of τ in both cases will correspond to $\sin\omega\tau$ equal 1, that is,

$$\omega^2<\omega^2(r), \quad \omega\tau=(2n+1)\pi+\tfrac{1}{2}\pi, \quad (64)$$

$$\omega^2>\omega^2(r), \quad \omega\tau=2n\pi+\tfrac{1}{2}\pi. \quad (65)$$

One thing may appear rather surprising in the preceding results, and that is the role played by frequencies of the order of $\sqrt{2}\omega_H$. If we refer to the electronic motions in the static magnetron, we notice that the electrons move around the filament with angular velocities ranging from 0 (near the filament) up to ω_H at a great distance from the filament [Eq. (15)]. None of these frequencies happens to play a role in the operation of sustaining oscillations, and the $\sqrt{2}\omega_H$ frequency is noticeably higher. This can be understood, as the angular velocities of the electrons cannot be observed in a magnetron whose anode is built as a complete cylinder around the filament. The only motions which may be noticed as giving a change in the anodic current are radial motions. The oscillations result, in this case, in electronic motions, where all electrons located on a certain cylindrical layer (at distance r_c) move together either to or fro, the whole cylindrical layer expanding or narrowing at one time. This is the type of motion corresponding to the frequency $\sqrt{2}\omega_H$, and it has nothing to do with the rotational frequency ω.

Another point to be emphasized is the great variety of conditions under which the magnetron is able to sustain oscillations. Conditions (62) and (64), for $\omega<\omega(r)$, and (63) and (65) for $\omega>\omega(r)$, offer a great number of different solutions, a characteristic almost never found in the discussion of electron tubes.

Where does the energy necessary for sustaining oscillations in the outer circuit come from? All our calculations refer to a magnetron very near its critical conditions ($I=0$). Such a magnetron stores up energy in kinetic form from the electrons rotating about the filament. In the process of sustaining oscillations in an outer circuit, some energy will be taken out of this reserve, thus slowing down the electrons; in order to keep the electron cloud in rotation, a small current I must be allowed to flow between anode and cathode, and the power IV supplied by the battery will restore the necessary energy and keep the cloud in steady rotation.

Our conclusion, that such a magnetron should be operated near $\sqrt{2}\omega_H$, fits with the results obtained by Blewett and Ramo[4] in a recent paper and is checked by experimental facts. Blewett and Ramo, however, failed to get the conditions for negative resistance, a difficulty they themselves emphasized at the end of their paper.

The first part of this paper, including Sections 1–4, was written in January, 1939, but its publication was delayed because of present circumstances. Several copies, however, were circulated; the author has to thank M. M. Blewett and Ramo for their courtesy in making reference to this unpublished paper.

[4] J. P. Blewett and S. Ramo, Phys. Rev. **57**, 635 (1940).

On the Dislocation Theory of Plastic Deformation

J. S. KOEHLER*
University of Pennsylvania, Philadelphia, Pennsylvania
(Received July 3, 1941)

A detailed study has been made of the lattice imperfections which are assumed to account for plastic deformation. Calculations of the strain energy associated with these dislocations have been made in the following cases: a dislocation in a uniform shear stress, two dislocations in an infinite medium, and a dislocation near a surface. The force acting on a dislocation is found by taking the gradient of the strain energy. A force is found which tends to attract dislocations toward the surface of a specimen. It is shown that about twice as much energy is required to produce a certain amount of slip inside a solid as is required to produce the same amount of slip at the surface. The energy required to produce a dislocation is found to be several electron volts per atomic plane, the exact amount depending on where it is located and how it was produced. Finally the energy stored in a material during work hardening is calculated by assuming that the dislocations are arranged in a regular two-dimensional lattice in the material. The density of dislocations found for severely work hardened material agrees with the predictions of other investigators. Numerical values found for the energy stored during work hardening are in agreement with experiment.

INTRODUCTION

IF a single crystal is subjected to a small tensile stress it will elongate according to Hooke's law. If the component of the shear stress acting along a definite crystallographic direction exceeds a certain critical value the crystal will also undergo considerable plastic deformation. For most crystals the value of the critical shear stress is about 10^7 dynes per cm^2. The permanent deformation apparently results from a sliding of sections of the crystal over one another. The sections are bounded by certain close-packed crystallographic planes and the slip takes place along the direction mentioned above. This slip direction is usually a direction in which the atoms are closely packed. A microscopic examination of a single crystal which has been elongated by several percent shows clearly the step-like discontinuities produced at the surface when slip occurs. The sections bounded by slip planes are several microns thick at room temperatures.

In a series of articles appearing in the *Journal of Applied Physics*, Seitz and Read[1] consider the various theories which have been used to discuss plastic deformation. They conclude that the theory of "dislocations" as developed by Taylor[2] yields the most satisfactory description of plastic phenomena which has been given to date. The present paper represents a further attempt to develop and to test the validity of dislocation theory. The predictions of dislocation theory which are considered in this paper are in good agreement with experiment.

According to Taylor, slip in a solid results from the motion of a certain type of lattice imperfection through the crystal. Taylor has used these "dislocations" to discuss qualitatively the hardening which occurs when crystals are plastically deformed. Recently Mott and Nabarro[3] using dislocation theory have discussed precipitation hardening.

In order to make clear the nature of a dislocation we consider a line dislocation in a simple cubic crystal. In Fig. 1 we have indicated the positions of the atoms in a crystallographic plane which is normal to the slip plane. The axis of the dislocation is perpendicular to the plane of the figure. Thus parallel atomic planes above and below the plane of the figure will have the same distribution of atoms about the center, or axis, of the dislocation. If a dislocation moves along its slip plane across the entire specimen, then Taylor has shown that the material above the slip plane will be displaced relative to the material below the slip plane by an amount equal to the lattice constant of the material.

An examination of Fig. 1 indicates that the distortion is just that which would be produced by inserting extra half-planes of atoms into

* Rackham Postdoctoral Fellow of the University of Michigan.

[1] F. Seitz and T. A. Read, J. App. Phys. **12**, 100, 170, 470 (1941).

[2] G. I. Taylor, Proc. Roy. Soc. **145**, 362 (1934).

[3] N. F. Mott and F. Nabarro, Proc. Phys. Soc. **52**, 86 (1940); F. Nabarro, Proc. Roy. Soc. **175**, 519 (1940).

an originally perfect crystal above the slip plane. Following Taylor we shall call this a positive dislocation. If the additional half-planes are inserted below instead of above the slip plane we shall call the dislocation which results a negative dislocation. Thus, if we are dealing with a positive dislocation we shall find that the material above the slip plane is compressed while the material below the slip plane has been dilated.

In the first section of this paper we shall calculate the force which acts on a dislocation when the material containing the dislocation is subjected to an external shearing force. Next, we shall consider two dislocations in an infinite medium. We shall determine the energy of the system and we shall evaluate the force acting between the dislocations. In the third section we shall discuss the case of a dislocation near a surface. Here too we shall calculate the energy of the system and the force acting on the dislocation. Finally, we shall evaluate the energy stored in a material when it is work hardened. All calculations made in this paper will use the theory of an elastic, isotropic continuum.

Dislocation in Uniform Shear Stress

According to dislocation theory an annealed specimen contains only a few line dislocations. If we apply a sufficiently large external shearing force to the specimen it will deform plastically. This deformation may take place either by the motion of existing dislocations or by the formation and motion of dislocations. In either case the force produced on an isolated dislocation by the external shearing force would be of interest. We shall, therefore, consider a line dislocation in a material which is also subjected to a uniform two-dimensional shear stress. This uniform shear stress is produced by the external force.

We shall first calculate the strain energy of the system. In order to calculate the strain energy we must know the stresses acting. It can be shown that the solution of certain two-dimensional problems of elasticity can be obtained by finding a suitable Airy stress function,[4] χ. This stress function must satisfy the differential equation

$$\frac{\partial^4\chi}{\partial x^4}+2\frac{\partial^4\chi}{\partial x^2\partial y^2}+\frac{\partial^4\chi}{\partial y^4}=0$$

and must yield stresses or displacements which satisfy the boundary conditions of the problem. The stresses are given by the following relations:

$$\sigma_x=\partial^2\chi/\partial y^2;\ \sigma_y=\partial^2\chi/\partial x^2;\ \tau_{xy}=-\partial^2\chi/\partial x\partial y. \quad (1)$$

The Airy stress function appropriate for this problem is[5]

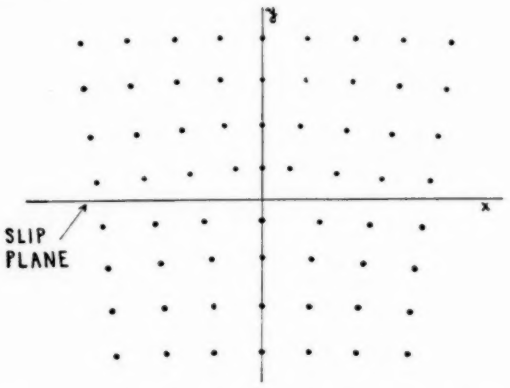

Fig. 1. Dislocation lying in a simple cubic crystal.

$$\chi=-Bxy-Dy\log(x^2+y^2)^{\frac{1}{2}}. \quad (2)$$

The first term represents the uniform shear stress; the second, as one can see from the displacements given below, represents a positive dislocation. The stresses resulting are

$$\begin{aligned}\sigma_x&=-Dy(3x^2+y^2)/(x^2+y^2)^2,\\ \sigma_y&=+Dy(x^2-y^2)/(x^2+y^2)^2,\\ \tau_{xy}&=+B+Dx(x^2-y^2)/(x^2+y^2)^2.\end{aligned} \quad (3)$$

The stresses due to the dislocation die off inversely as the first power of the distance from the center of the dislocation. The displacements can now be calculated from Hooke's law. They are

$$\begin{aligned}u&=\frac{(m-1)}{mG}D\tan^{-1}\left(\frac{y}{x}\right)+\frac{D}{2G}\frac{xy}{x^2+y^2},\\ v&=-\frac{(m-2)}{2mG}D\log(x^2+y^2)^{\frac{1}{2}}-\frac{D}{2G}\frac{x^2}{x^2+y^2}.\end{aligned} \quad (4)$$

[4] S. Timoshenko, *Theory of Elasticity* (McGraw-Hill Book Co., Inc., 1934), p. 25.

[5] This dislocation differs from the one used by Taylor. Dislocations of this type were probably first used to discuss plastic deformation by J. M. Burgers and W. G. Burgers. J. M. Burgers, Proc. K. Akad. Amst. **42**, 263, 378 (1939). We shall discuss the differences between these two types of dislocations near the end of the next section.

Here u is the displacement in the x direction and v is the displacement in the y direction. G is the shear modulus of the material, and m is the reciprocal of Poisson's ratio. If we measure the angle appearing in the equation for u from the plus x axis then the displacements are discontinuous along this axis. The material just below the positive x axis is displaced in the x direction with respect to the material just above the axis by an amount

$$\lambda=2\pi(m-1)D/mG, \qquad D=mG\lambda/2\pi(m-1). \quad (5)$$

According to Eqs. (3) and (4) the stresses and the displacements are singular at the center of the dislocation. Physically this means that an elastic continuum theory is not capable of describing the situation near the center of a dislocation. We shall, therefore, in all problems surround the axis of each dislocation by a cylinder of radius r_0. We shall choose r_0 so that the maximum strain at the surface of the cylinder is one-tenth. We shall consider only situations in which all dislocations, impurity atoms, precipitates and other singularities are separated from the dislocation in question by distances which are large compared with r_0. For such systems the stress at r_0 will be, to a good approximation, just the stress produced by the dislocation. Furthermore, the interaction energies and the forces exerted by other singularities on the dislocation will depend upon the strain energy in the material outside r_0 since the strain energy inside r_0 will not change appreciably if the dislocation is moved relative to the other singularities.

Let us calculate r_0 in the case of copper. We shall take λ of Eq. (5) to be the translation which would carry an atom of copper from a cube corner to the center of a cube face. This unit slip distance is 2.55×10^{-8} cm in copper. Using $G=4.53\times10^{11}$ dynes per cm^2 and $m=2.941$ we find from Eq. (5) that $D=2.78\times10^{3}$ dynes per cm. The shear strain is found to be the largest strain. Using Hooke's law and substituting from Eqs. (3) we find

$$\gamma_{xy}=\tau_{xy}/G=+Dx(x^2-y^2)/G(x^2+y^2)^2,$$

where γ_{xy} is the shear strain. Putting in the limiting value of one-tenth for γ_{xy} and inserting the maximum value that the expression on the right has on the surface of the cylinder we find

$$r_0=D/\gamma_{xy\,\max}\,G=6.15+10^{-8}\text{ cm for copper.} \quad (6)$$

The strain energy of a slab of material of unit thickness in the z direction is[6]

$$W=\int\int\frac{ds}{4G}\left\{\frac{(m-1)}{m}(\sigma_1+\sigma_2)^2-2\sigma_1\sigma_2+2\tau_{12}^2\right\}, \quad (7)$$

where m is the reciprocal of Poisson's ratio and where we have assumed that the material is in a state of a plane strain. Equation (7) gives the strain energy in any orthogonal two-dimensional coordinate system. In this equation ds is the element of area and σ_1, σ_2, and τ_{12} are the stresses in the coordinate system chosen. Substituting from Eqs. (3) we find

$$W=\frac{1}{2G}\int\int dxdy\left\{B^2+\frac{D^2}{x^2+y^2}+\frac{2BDx(x^2-y^2)}{(x^2+y^2)^2}\right\}. \quad (8)$$

It is apparent from Eq. (8) that if either the uniform shear stress or the dislocation is present in the specimen it will contain strain energy. If both the uniform shear stress and the dislocation are present simultaneously, the strain energy is not simply the sum of the strain energy due to a uniform shear stress and the strain energy due to a dislocation. In addition to these self-energies we have a cross term, an interaction energy. The first two terms of the integral (8) are self-energy terms while the last term is the interaction energy in which we are interested. In order to get a sensible result one must be careful about the limits of integration. The interaction energy can be written as

$$W_{\text{int}}=\frac{2BD}{G}\left\{\int_{r_0}^{c}\int_{-c+\xi}^{-r_0}\frac{x(x^2-y^2)}{(x^2+y^2)^2}dxdy+\int_{r_0}^{c}\int_{r_0}^{c+\xi}\frac{x(x^2-y^2)}{(x^2+y^2)^2}dxdy\right\}. \quad (9)$$

In this expression C is a large distance which is

[6] E. Trefftz, *Handbuch der Physik*, Vol. VI, p. 79 (1928).

allowed to approach infinity after the integration has been carried out. The result then becomes

$$W_{\text{int}} = -2BD\xi/G. \tag{10}$$

The distance ξ essentially measures the position of the dislocation with respect to the field of uniform shear. The force acting on the dislocation is given by the negative of the derivative of this expression with respect to ξ.

$$F = +2BD/G. \tag{11}$$

The force acts in the plus x direction on this positive dislocation.

Using the value of D for a unit dislocation in copper and assuming that the uniform shear stress is 10^7 dynes per cm (i.e., the value of the critical shear stress for copper) we find the force to be 2.22×10^{-9} dyne for a segment whose length is the distance between successive atomic planes which are perpendicular to the axis of the dislocation. This force is very small compared with chemical forces.

Two Parallel Line Dislocations

In this section we shall calculate the strain energy associated with two parallel line dislocations in an isotropic, continuous medium. Quantitative values of the strain energy and of the force acting between the dislocations will be given. Finally, Taylor's treatment of dislocation theory will be discussed.

The Airy stress function for two unlike dislocations of equal strength in an infinite medium is

$$\chi = D\{y\log(x^2+y^2)^{\frac{1}{2}} - (y-y_0)\log[(x-x_0)^2+(y-y_0)^2]^{\frac{1}{2}}\}. \tag{12}$$

We have assumed that the negative dislocation has its center at the origin of our coordinate system. The positive dislocation has its center at x_0y_0. Each dislocation has associated with it a slip plane which passes through the center of the dislocation and is parallel to the xz plane (z is normal to the plane of Fig. 1). The stresses obtained from (12) are

$$\begin{aligned}
\sigma_x &= D\left\{\frac{y(3x^2+y^2)}{(x^2+y^2)^2} - \frac{(y-y_0)(3\{x-x_0\}^2+\{y-y_0\}^2)}{(\{x-x_0\}^2+\{y-y_0\}^2)^2}\right\},\\
\sigma_y &= -D\left\{\frac{y(x^2-y^2)}{(x^2+y^2)^2} - \frac{(y-y_0)(\{x-x_0\}^2-\{y-y_0\}^2)}{(\{x-x_0\}^2+\{y-y_0\}^2)^2}\right\},\\
\tau_{xy} &= -D\left\{\frac{x(x^2-y^2)}{(x^2+y^2)^2} - \frac{(x-x_0)(\{x-x_0\}^2-\{y-y_0\}^2)}{(\{x-x_0\}^2+\{y-y_0\}^2)^2}\right\}.
\end{aligned} \tag{13}$$

From Eqs. (12) and (13) one sees that if the two dislocations coincide they will neutralize one another leaving an unstrained crystal.

Substituting the stresses given in Eqs. (13) into expression (7) we obtain the strain energy for an infinite slab of material which is of unit thickness in the z direction:

$$\begin{aligned}
W = \frac{D^2}{2G}\int\int dxdy\Bigg\{&\frac{2(m-1)}{m}\left[\frac{y^2}{r_1^4}+\frac{(y-y_0)^2}{r_2^4}-\frac{2y(y-y_0)}{r_1^2r_2^2}\right]+\frac{x^2-y^2}{r_1^4}+\frac{\{x-x_0\}^2-\{y-y_0\}^2}{r_2^4}\\
&-\frac{2x(x-x_0)(x^2-y^2)(\{x-x_0\}^2-\{y-y_0\}^2)}{r_1^4r_2^4}-\frac{y(y-y_0)(x^2-y^2)(3\{x-x_0\}^2+\{y-y_0\}^2)}{r_1^4r_2^4}\\
&-\frac{y(y-y_0)(3x^2+y^2)(\{x-x_0\}^2-\{y-y_0\}^2)}{r_1^4r_2^4}\Bigg\},
\end{aligned} \tag{14}$$

where

$$r_1 = (x^2+y^2)^{\frac{1}{2}}, \quad r_2 = [(x-x_0)^2+(y-y_0)^2]^{\frac{1}{2}}.$$

Let us surround the axis of each dislocation by a cylinder of radius r_0 and proceed with the integration of Eq. (14) over the portions of the slab which lie outside these cylinders. The terms in Eq. (14) can be divided into two classes. First, there are the self-energy terms which contain r_1 or r_2. Second, there are the interaction terms which contain both r_1 and r_2. The self-energy terms can be integrated immediately and yield

$$W_{\text{self}}=\frac{2\pi D^2(m-1)}{mG}\log\frac{L}{r_0}, \tag{15}$$

where L is essentially the radius of our cylindrical specimen which has the two dislocations near its center. We introduce new Cartesian coordinates into the interaction terms taking the origin midway between the two dislocations. The new coordinates ζ and η are given by

$$x=\zeta\cos\phi-\eta\sin\phi+\tfrac{1}{2}R\cos\phi,\quad y=\zeta\sin\phi+\eta\cos\phi+\tfrac{1}{2}R\sin\phi, \tag{16}$$

where

$$R=(x_0^2+y_0^2)^{\frac{1}{2}},\quad \tan\phi=y_0/x_0.$$

The interaction terms can then be written:

$$W_{\text{int}}=-\frac{D^2}{2G}\int\int d\zeta d\eta\left\{\frac{4(m-1)}{m}\left[\frac{\zeta^2\sin^2\phi+\eta^2\cos^2\phi-\frac{1}{4}R^2\sin^2\phi}{\zeta^4+2\zeta^2(\eta^2-\frac{1}{4}R^2)+(\eta^2+\frac{1}{4}R^2)^2}\right]\right.$$
$$+\frac{\zeta^6\cos2\phi+\zeta^4(\eta^2\cos2\phi-\frac{3}{4}R^2\cos2\phi)+\zeta^2(-\eta^4\cos2\phi-\eta^2R^2[4+2\cos2\phi]+[3R^4\cos2\phi/16])}{[\zeta^4+2\zeta^2(\eta^2-\frac{1}{4}R^2)+(\eta^2+\frac{1}{4}R^2)^2]^2}$$
$$\left.+\frac{(-\eta^6\cos2\phi+\eta^4\tfrac{1}{4}R^2[-4+2\cos2\phi]+\eta^2\tfrac{1}{16}R^4[4+\cos2\phi]-[R^6\cos2\phi/64])}{[\zeta^4+2\zeta^2(\eta^2-\frac{1}{4}R^2)+(\eta^2+\frac{1}{4}R^2)^2]^2}\right\}. \tag{17}$$

In Eq. (17) we have omitted terms that are odd in ζ or η since these would obviously not contribute to the integral. If we now integrate Eq. (17) over the region outside the cylinders we obtain the interaction energy. Adding this interaction energy to the self-energy we find that the total, elastic, strain energy of the positive and negative dislocation in an infinite medium is

$$W=\frac{mG\lambda^2}{2\pi(m-1)}\log\frac{R}{2r_0}-\frac{m^2G\lambda^2}{4\pi(m-1)^2}[\cos2\phi-\tfrac{1}{2}]. \tag{18}$$

Expression (18) is approximate since we have neglected small terms of order $(m^2G\lambda^2/4\pi(m-1)^2)\times(r_0^2/R^2)$. The force acting on the positive dislocation at x_0y_0 has the components

$$F_R=-\frac{mG\lambda^2}{2\pi(m-1)}\frac{1}{R},$$
$$F_\phi=-\frac{m^2G\lambda^2}{2\pi(m-1)^2}\frac{\sin2\phi}{R}. \tag{19}$$

Numerical values of the strain energy and the force acting between dislocations have been calculated for various distances of separation in copper. The results are given in Figs. 2, 3, and 4. In Fig. 2 we have given the strain energy in a slab whose thickness is the distance between successive atomic planes which are perpendicular to the axis of the dislocation. In Figs. 3 and 4 we have given the force acting on a dislocation segment whose length is equal to the thickness of the slab just mentioned. In Fig. 4 we have given that component of the force between two dislocations which acts along the slip direction. We have assumed that the slip planes of the two dislocations being considered are separated by by 10^{-6} cm.

We are now in a position to discuss some of the differences between the dislocation theory developed by Taylor and the dislocation theory used in the present paper. Imperfections of the type shown in Fig. 1 can be obtained in elastic

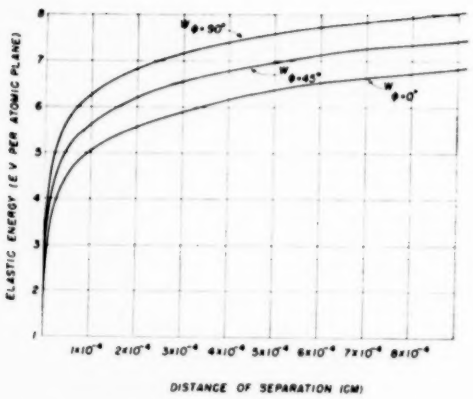

FIG. 2. Strain energy for various distances of separation in copper.

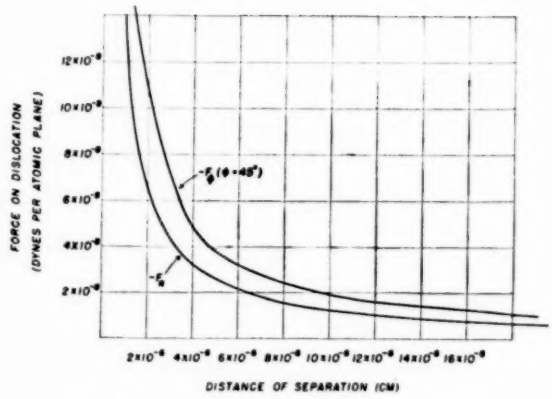

FIG. 3. Force acting on dislocation segment.

theory if one uses the following stress function:

$$\chi = Ay \log(x^2+y^2)^{\frac{1}{2}} + Bx \tan^{-1}(y/x). \quad (20)$$

The strength and nature of the dislocation represented by the above function are determined by the values assigned to the constants A and B. If we put $A=B=-\lambda G/\pi$ then we are dealing with a positive Taylor dislocation whose slip distance is λ. If we take $A=-mG\lambda/2\pi(m-1)$ and $B=0$ we are dealing with a positive Burgers dislocation whose slip distance is also λ.

We have not used Taylor dislocations for the following reason. Suppose we have a block which is finite in the x and y directions and which contains a dislocation. Let us take the surface of the block to be free from external forces. Then it can be shown that the boundary conditions which apply to this problem can only be satisfied if one takes the dislocation to be a Burgers dislocation.

In any dislocation theory it is important to decide how a dislocation will move along its slip plane under the influence of various stress fields which may be present in the material. Taylor treats the problem in the following way. Consider a positive dislocation located at the origin of a coordinate system. The xz plane will be taken to be the slip plane and the x axis the slip direction. Taylor, Burgers, and Mott and Nabarro assume that this positive dislocation will move in the plus x direction if the total external shear stress acting at the origin in that direction is greater than zero. If the above assumption is valid it would be most reasonable to assume further that the force tending to move a dislocation in a given direction is proportional to the external shear stress which acts in that direction at the center of the dislocation. This last assumption can be shown to be in error in the following way. If the assumption is used to calculate the force acting between two Burgers dislocations the result found does not agree in form with the force obtained by calculating the strain energy of the system. If one considers Taylor dislocations in various stress fields then the assumption gives the correct form for the forces, but the constant of proportionality seems to depend upon the particular stress system being considered. For example, one finds that

$$2F_A/\tau_A = F_B/\tau_B. \quad (21)$$

Here F_A is the force acting on a positive Taylor dislocation in a uniform shear stress; τ_A is the value of the uniform shear stress at the center of the dislocation. F_B is the force acting between a positive Taylor dislocation and an equal negative Taylor dislocation; τ_B is the shear stress produced at the center of the positive dislocation by the nearby negative dislocation. These forces are obtained by calculating the strain energy of the system considered.

In spite of the discussion which we have just given it can be seen that the results of Taylor's theory are qualitatively correct. This is true because Taylor assumed an interaction between two dislocations which is essentially of the correct form (i.e. the force dies off inversely as the first power of the distance between the dislocations). The error resulting from the use of the wrong

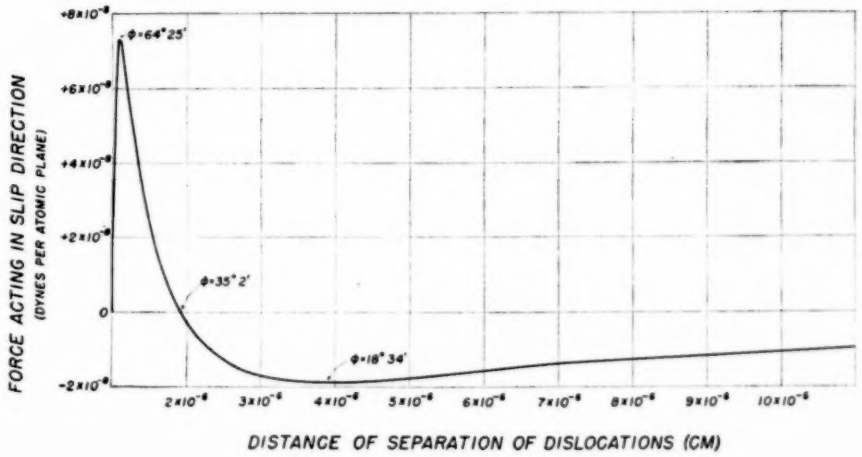

FIG. 4. Force between two dislocations in direction of slip.

type of dislocation causes Taylor to overestimate the critical shear stress by a factor of about $4(m-1)/m$. For copper this factor has the value 2.64. Our discussion indicates that Taylor's method of determining when a dislocation will move may also be in error. If this is true then Eq. (21) allows us to estimate the error made. Such an error would cause Taylor to underestimate the critical shear stress by a factor of about two. Thus Taylor's results are not in error by more than a factor three.

A Dislocation in a Cylinder

There are two ways in which dislocations could be formed. First, dislocation pairs could be created inside the specimen. Each dislocation pair would consist of a positive and a negative dislocation. Secondly, single dislocations may be formed at the surface of the material. In order to consider these possibilities in detail we shall calculate the strain energy and the force acting on a dislocation near a surface. Finally we shall discuss briefly the annealing process in metals.

Let us consider a dislocation in a circular cylinder of radius ρ. We shall suppose that the dislocation is not in general at the center of the cylinder. We shall take the axis of the dislocation parallel to the axis of the cylinder. The symmetry of this problem is that of two eccentric cylinders. Problems of this type can be conveniently treated using bipolar coordinates. G. B. Jeffery[7] has used this orthogonal system of coordinates to treat two-dimensional elastic problems and we shall use many of his results. The curvilinear coordinates are defined by the relation

$$\alpha+i\beta\equiv\log\left\{\frac{x+i(y+c)}{x+i(y-c)}\right\}, \tag{22}$$

where c is a real positive constant and x and y are Cartesian coordinates. Solving for x and y we find

$$x=c\sin\beta/(\cosh\alpha-\cos\beta),$$
$$y=c\sinh\alpha/(\cosh\alpha-\cos\beta). \tag{23}$$

The points $0,+c$ and $0,-c$ are the two poles of the system. It is clear that if we keep β fixed and change α by an amount $d\alpha$ we shall traverse a distance

$$d\alpha/h=cd\alpha/(\cosh\alpha-\cos\beta)$$

similarly if we keep α fixed and change β by $d\beta$ we shall move through the distance $d\beta/h$. Figure 5 shows the two orthogonal families of circles that form this curvilinear coordinate net.

Let us suppose that the dislocation is at the pole which lies at $0,+c$. The surface of the material will be represented by the circle on which $\sinh\alpha=c/\rho$. If the surface of the cylinder is to be free from external forces the boundary conditions which the stresses must fulfill are

$$\sigma_\alpha=0, \qquad \tau_{\alpha\beta}=0 \tag{24}$$

on the cylinder having $\sinh\alpha=c/\rho$. We shall try a stress function which we believe to be appropriate for this problem. We put

$$\chi=\frac{D\sin\beta}{h}\{\alpha+\tfrac{1}{2}\exp[-2(\alpha-\alpha_1)]\}, \tag{25}$$

[7] G. B. Jeffery, Trans. Roy. Soc. **221**, 265 (1920). See also E. Coker and L. Filon, *Photoelasticity* (Cambridge University Press, 1931).

where α_1 is defined by $\sinh\alpha_1 = c/\rho$. If the first term of this expression is transformed into Cartesian coordinates we find that it represents a positive dislocation at $0, +c$ and a negative, "image" dislocation at $0, -c$. This stress function is a linear combination of terms which Jeffery has shown satisfy Airy's equation. Jeffery has also given relations which enable one to calculate the stresses in bipolar coordinates once the stress function is known. Using these we find

$$\sigma_\alpha = -\frac{D\sinh\alpha\sin\beta}{c}\{1-\exp[-2(\alpha-\alpha_1)]\},$$

$$\sigma_\beta = +\frac{D\sin\beta}{c}\{2(\cosh\alpha-\cos\beta)\exp[-2(\alpha-\alpha_1)]-\sinh\alpha[1-\exp[-2(\alpha-\alpha_1)]]\}, \tag{26}$$

$$\tau_{\alpha\beta} = -\frac{D\cos\beta}{c}(\cosh\alpha-\cos\beta)\{1-\exp[-2(\alpha-\alpha_1)]\}.$$

It is at once evident that these stresses satisfy the boundary conditions given above.

We can now calculate the strain energy. Substituting the stresses into Eq. (7) we obtain

$$W = \frac{D^2}{2G}\int_{\alpha_1}^{\alpha_0}\int_{-\pi}^{\pi} d\alpha d\beta\Big[2(m-1)\sin^2\beta\exp[-4(\alpha-\alpha_1)]+m\cos^2\beta\{1-\exp[-2(\alpha-\alpha_1)]\}^2$$
$$-\frac{2(m-2)\sinh\alpha\exp[-2(\alpha-\alpha_1)]\{1-\exp[-2(\alpha-\alpha_1)]\}\sin^2\beta}{\cosh\alpha-\cos\beta}$$
$$+\frac{(m-2)\sinh^2\alpha\sin^2\beta\{1-\exp[-2(\alpha-\alpha_1)]\}^2}{(\cosh\alpha-\cos\beta)^2}\Big].$$

In this equation we do not integrate α to plus infinity because, just as in our previous problems, we find that elastic theory is not able to describe the distortion of the material near the center of the dislocation. Instead we put $\sinh\alpha_0 = c/r_0$. Carrying out the integrations we find

$$W = \frac{mG\lambda^2}{4\pi(m-1)^2}\Big[(m-1)\alpha+\tfrac{1}{2}(m-2)\sinh\alpha\{\sinh\alpha-\cosh\alpha\}+\left(\frac{3m-4}{2}\right)\exp[-2(\alpha-\alpha_1)]$$
$$-\left(\frac{3m-4}{4}\right)\exp[-4(\alpha-\alpha_1)]-\left(\frac{m-2}{2}\right)\exp[-4\alpha+2\alpha_1]+\left(\frac{m-2}{4}\right)\exp[-6\alpha+4\alpha_1]\Big]_{\alpha_1}^{\alpha_0}. \tag{27}$$

Let us rewrite this equation in a more useful form for the special case of a dislocation inside the plane face of an infinite block of material. We find that, to a good approximation,

$$W = \frac{mG\lambda^2}{4\pi(m-1)}\log\frac{2R}{r_0}+\text{surface terms}, \tag{28}$$

where R is the distance of the dislocation from the surface of the cylinder. The first term is the leading term in this expression. This term represents the strain energy in the block due to the stresses produced by the dislocation and the "image" dislocation which is a distance R outside the plane face. The use of an "image" dose not

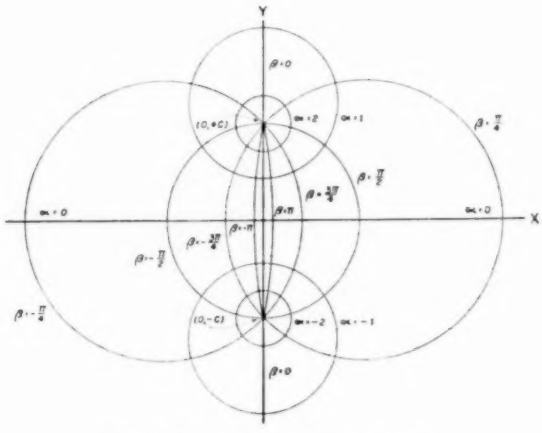

FIG. 5. Bipolar coordinate system.

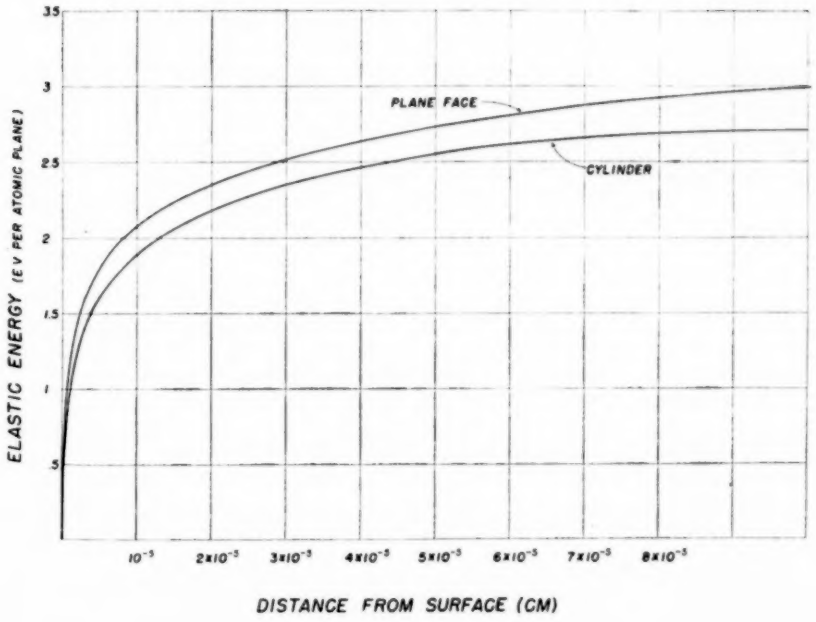

FIG. 6. Strain energy as a function of distance from surface.

completely satisfy the boundary conditions at the plane face and the additional stresses used produce the "surface terms" in the strain energy. These "surface terms" are almost independent of the distance of the dislocation from the surface except at small distances. Because of this the first term increases in importance as the dislocation moves away from the surface. If we consider a very large copper block which has a dislocation 5×10^{-7} cm inside a plane face we find that the surface terms are 26 percent of the image term. If the dislocation is 10^{-4} cm from the surface, the surface terms amount to 8 percent of the image term. The force acting on the dislocation is obtained by taking the derivative of the strain energy with respect to the distance from the surface. The result for the case of a dislocation inside a plane surface is

$$F=-\frac{mG\lambda^2}{4\pi(m-1)}\frac{1}{R}+\text{surface terms.} \quad (29)$$

The curves drawn in Figs. 6 and 7 give the strain energy and the force acting on a dislocation as a function of its distance from the surface in a copper block. We have considered two cases, one in which we have a dislocation near the plane face of a semi-infinite block, another in which we have a dislocation in a cylinder of radius 10^{-4} cm. In the second case the strain energy reaches a maximum when the dislocation is at center of the cylinder. The strain energy curve is symmetrical about this maximum. Instead of plotting the elastic energy of a slab of unit thickness, we have given the elastic energy in a slab whose thickness is the distance between successive atomic planes which are perpendicular to the axis of the dislocation.

We can now decide whether it is energetically easier to form dislocations at surfaces or in pairs inside the specimen. In order to make a comparison we shall suppose that slip of one atomic unit has occurred in both cases along a distance R in the slip direction. For a dislocation near a surface, R is the distance from the center of the dislocation to the surface. In the case of two dislocations inside an infinite block, R is the distance between the dislocations. By comparing the curves of Fig. 6 with that of Fig. 2 one finds that, in general, it requires about twice as much energy to produce a pair of dislocations as it takes to form a single dislocation near the surface. This does not necessarily mean that most of the dislocations are formed at the surface of the specimen. One must also remember that there is, in general, a much larger volume in which dislocations can be formed inside the material than there is near the surface.

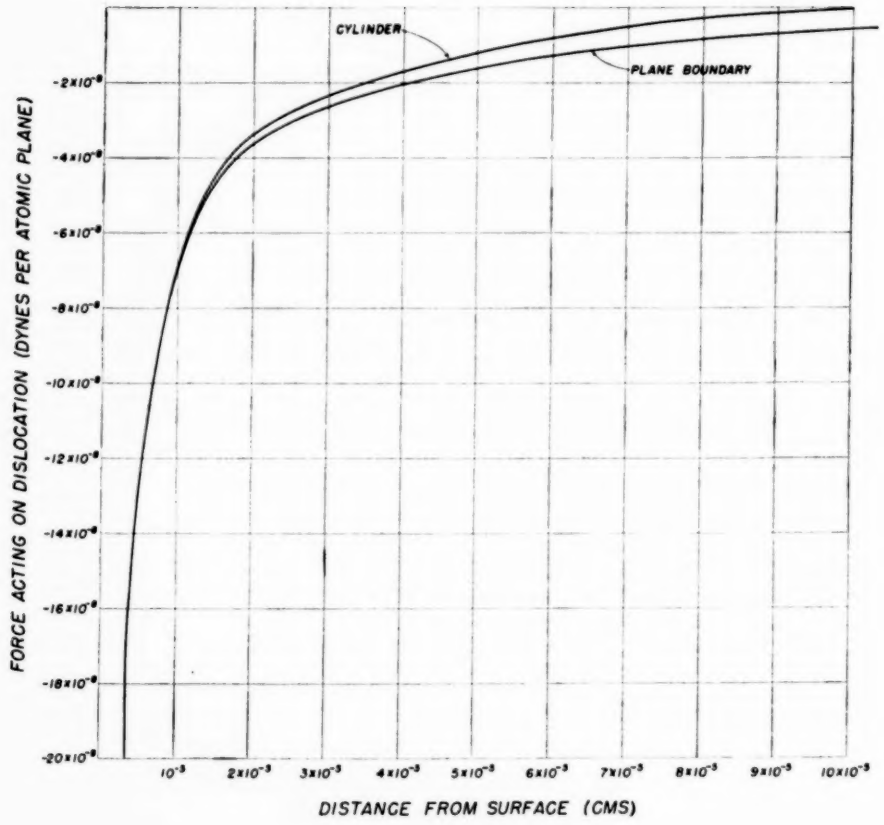

FIG. 7. Force on dislocation as a function of distance from surface.

If dislocation theory is correct, then the forces investigated in this section and in the previous one will be of great importance for any theory of annealing. Taylor has shown that a substance containing a large number of dislocations is hard. However, if we have a specimen which initially contains a large number of dislocations per cm², then the image force acting toward the surface will cause dislocations to move out of the specimen. If we have positive and negative dislocations inside the specimen which are on the same slip plane, they can attract and annihilate one another. Unfortunately, the experimental data in this particular field are not sufficient for a quantitative test of the theory. Further data on resoftening temperatures for single crystals, on the effect of small amounts of soluble impurities on the resoftening temperatures of single crystals, and studies of the effect of the size of the single crystal on resoftening would be valuable. Measurements of the internal friction as a function of the time for material having a decrement of about 10^{-4} on small single crystals of various sizes would also be of interest.

THE ENERGY STORED DURING WORK HARDENING

Experimentally it is found that if a metal is severely cold worked a certain amount of energy is stored in the metal. This energy can be released by heating the material. Taylor and Quinney[8] have made measurements on the amount of energy stored in this way. In this section we should like to see if we can check their results using dislocation theory.

We shall assume that a work hardened material contains many positive and negative dislocations which are arranged in a two-dimensional lattice. We shall first calculate the total energy of a dislocation pair in the rectangular lattice shown in Fig. 8. The elastic energy required to form a dislocation pair whose distance

[8] G. I. Taylor and H. Quinney, Proc. Roy. Soc. **143**, 307 (1934); **163**, 157 (1937).

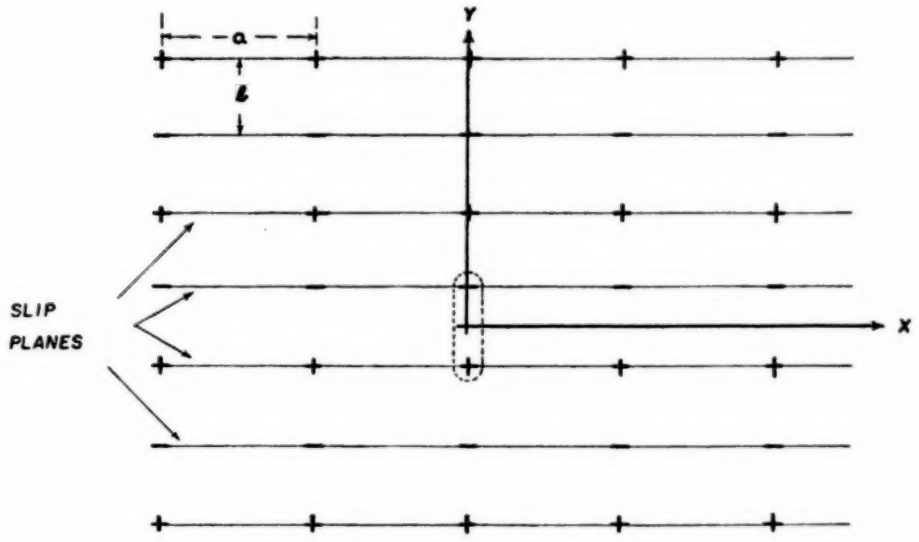

FIG. 8. Rectangular lattice and slip planes.

of separation is R is given by Eq. (18) as

$$W=\frac{mG\lambda^2}{2\pi(m-1)}\log\frac{R}{2r_0}$$

$$-\frac{m^2G\lambda^2}{4\pi(m-1)^2}[\cos 2\phi-\tfrac{1}{2}]. \quad (30)$$

The energy of a dislocation pair in a lattice is the energy required to form an isolated pair minus the binding energy of the pair in the lattice. The interaction of two dislocations is given by a logarithmic potential such as is shown above. The above relation includes not only the interaction between the two dislocations, but also the self-energy of the dislocations.

Let us calculate the interaction energy between the dislocation pair located at the origin and the pair located at $x=0$, $y=2nb$ (see Fig. 8). We shall assume that the members of each pair are separated by a distance b. The energy which the system acquires because of the presence of the positive dislocation at $0,-b/2$ in the field of the pair at 0, $2nb$ is

$$W_+=\frac{mG\lambda^2}{2\pi(m-1)}\log\left(\frac{2nb+b}{2nb}\right).$$

The energy which the system acquires because of the presence of the negative dislocation near the origin in the field of the pair at 0, $2nb$ is

$$W_-=\frac{mG\lambda^2}{2\pi(m-1)}\log\left(\frac{2nb-b}{2nb}\right).$$

Thus the interaction energy of the two pair of dislocations is

$$W_1=-\frac{mG\lambda^2}{2\pi(m-1)}\log\left(\frac{4n^2}{4n^2-1}\right). \quad (31)$$

It is evident that W_1 vanishes when n approaches infinity. W_1 is therefore an interaction energy, not a self-energy. Using this expression we can calculate the interaction energy between the pair at the origin and all other pairs in the plane $x=0$. We find

$$W_2=-\frac{mG\lambda^2}{\pi(m-1)}\sum_{n=1}^{\infty}\log\left(\frac{4n^2}{4n^2-1}\right). \quad (32)$$

We should like to calculate the interaction energy between the pair at the origin and the dislocations in the plane for which $x=+\tau a$. In making this calculation we shall use Eq. (30) to obtain the interaction energy of two dislocations. In using Eq. (30) for any two dislocations of the lattice we shall assume that ϕ remains constant although R may change. When the lattice of dislocations is considered we may there-

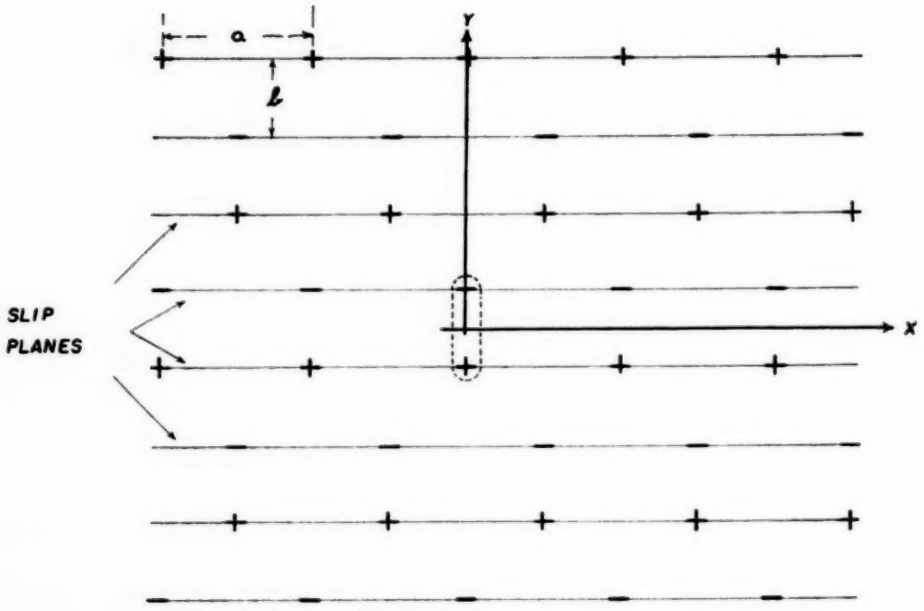

FIG. 9. Dislocations in rectangular lattice.

fore vary the distance of separation of the dislocations, but not the angles of the lattice. The resulting interaction potential has exactly the same form as the electrostatic interaction of two long, parallel, uniformly charged rods. Madelung[9] has calculated the potential due to a plane lattice of positively charged lines. Using his result we find that the interaction energy between the positive dislocation at $x=0$, $y=-\frac{1}{2}b$ and the positive dislocations in the plane at $x=+\tau a$ is

$$W_3=\frac{mG\lambda^2}{2\pi(m-1)}\sum_{l=1}^{\infty}\frac{e^{-\pi l\tau a/b}}{l}\cos\left\{\frac{\pi l(-\frac{1}{2}b+\frac{1}{2}b)}{b}\right\}-\frac{mG\lambda^2\tau a}{(m-1)b}+K,$$

where K is a constant. Similarly the interaction energy between the negative dislocations in the plane $x=+\tau a$ and the positive dislocation being considered is:

$$W_4=-\frac{mG\lambda^2}{2\pi(m-1)}\sum_{l=1}^{\infty}\frac{e^{-\pi l\tau a/b}}{l}\cos\left\{\frac{\pi l(-\frac{1}{2}b-\frac{1}{2}b)}{b}\right\}+\frac{mG\lambda^2\tau a}{(m-1)b}-K.$$

The total interaction energy of the positive dislocation with dislocations in the plane $x=\tau a$ is

$$W_5=\frac{mG\lambda^2}{2\pi(m-1)}\sum_{\substack{l=1\\ l\text{ is odd}}}^{\infty}\frac{2e^{-\pi l\tau a/b}}{l}. \tag{33}$$

With this result we find the total interaction energy of the positive dislocation with dislocations in all planes except the plane having $x=0$ is

$$W_6=\sum_{\tau=1}^{\infty}2W_5=\frac{2mG\lambda^2}{\pi(m-1)}\sum_{\tau=1}^{\infty}\sum_{\substack{l=1\\ l\text{ is odd}}}^{\infty}\frac{e^{-\pi l\tau a/b}}{l}. \tag{34}$$

The sum over l can be carried out and we find that Eq. (34) becomes

$$W_6=\frac{mG\lambda^2}{\pi(m-1)}\sum_{\tau=1}^{\infty}\log\left(\frac{1+e^{-\pi\tau a/b}}{1-e^{-\pi\tau a/b}}\right). \tag{35}$$

[9] E. Madelung, Physik. Zeits. **19**, 527 (1918).

TABLE I. *Data used in calculations.*

	NaCl	Cu	Al	Ni	Fe
Slip direction	(110)	(110)	(110)	(110)	(111)
Modulus of rigidity $\times 10^{-11}$ (dynes/cm^2)	1.872	4.53	2.665	7.69	8.114
Poisson's ratio	0.2053	0.340	0.343	0.309	0.280
r_0(A)	7.969	6.15	6.90	5.71	5.48
λ(A)	3.979	2.552	2.855	2.480	2.478
Density (g/cm^3)	2.165	8.93	2.699	8.80	7.865

TABLE II. *Results of calculations.*

	Cu	Al	Ni	Fe
Spacing (a) (Rectangular lattice)	34.72	32.38	35.75	29.99
Spacing (a) (Diagonal lattice)	29.24	27.26	30.18	25.03
Energy stored (cal./g) (Rectangular lattice)	0.518	1.013	0.851	0.963
Energy stored (cal./g) (Diagonal lattice)	0.507	1.130	0.832	0.942
Energy stored (cal./g) (Experimental value)	0.5	1.1	0.78	1.2

We now note that the interaction energy of the negative dislocation at $x=0$, $y=+\frac{1}{2}b$ with dislocations in all planes except the plane having $x=0$ is equal to the interaction energy of the positive dislocation as given in Eq. (35). Thus using Eqs. (30), (32), and (35) the total energy required to form a pair of dislocations in a rectangular lattice is found to be:

$$W_{\text{pair}}=\frac{mG\lambda^2}{2\pi(m-1)}\left[\log\frac{b}{2r_0}+\frac{3m}{4(m-1)}-2\sum_{n=1}^{\infty}\log\left(\frac{4n^2}{4n^2-1}\right)+4\sum_{r=1}^{\infty}\log\left(\frac{1+e^{-\pi ra/b}}{1-e^{-\pi ra/b}}\right)\right]. \tag{36}$$

This is not yet complete since we must add to this twice the energy required to distort the material inside a cylinder of radius r_0 around the center of a dislocation. This cannot be calculated from elastic theory. However, H. B. Huntington[10] has made a calculation of this energy using atomic concepts. He found the energy inside a cylinder of radius r_0 to be about 0.8 ev per atomic plane in the case of sodium chloride. We can estimate the value of this energy in other materials in the following way. It is assumed that the strain energy inside the cylinder of radius r_0 is proportional to the strain energy outside the cylinder in the case of an isolated dislocation. The constant of proportionality is taken to be the same for all materials and is determined by using Huntington's value for the energy inside the cylinder in the case of sodium chloride. For a dislocation at the center of a cylinder of material of radius 10^{-4} cm, there is about four times as much strain energy outside r_0 as there is inside.

It will be noticed that the rectangular lattice of dislocations is not stable. The lattice planes parallel to the $x=0$ plane repel one another and the lattice tends to spread out in the x direction. This is not a really serious difficulty for two reasons. First, there exists a small periodic potential of atomic origin which probably prevents dislocations from moving along the slip planes unless some external stress is present. Second, the actual lattice of dislocations cannot be very stable because resoftening takes place in some materials at room temperature. Extensive resoftening can be brought about in a single crystal of aluminum by heating it to 600°C. The lattice cannot decrease its energy by making b smaller because dislocations can only move along slip planes, not perpendicular to them. Thus b is determined by the way in which the dislocations are formed.

We have also made calculations for a lattice which is more stable than the rectangular lattice. The arrangement of dislocations in this lattice is shown in Fig. 9. The calculation of the energy required to produce a pair of dislocations in such a lattice is performed in exactly the same manner as the calculation for the rectangular lattice. The energy of a pair of dislocations in this case is

$$W_{\text{pair}}=\frac{mG\lambda^2}{2\pi(m-1)}\left[\log\frac{b}{2r_0}+\frac{3m}{4(m-1)}-2\sum_{\substack{n=2\\ n\text{ even}}}^{\infty}\log\left(\frac{4n^2}{4n^2-1}\right)+2\sum_{r=1}^{\infty}\log\left(\frac{1+e^{-\pi ra/b}}{1-e^{-\pi ra/b}}\right)\right.$$
$$\left.-2\sum_{\substack{s=1\\ s\text{ odd}}}^{\infty}\log\left(\frac{1+e^{-\pi sa/4b}}{1-e^{-\pi sa/4b}}\right)\right]. \tag{37}$$

[10] H. B. Huntington, Phys. Rev. **59**, 942A (1941).

The above equation gives a pair energy which is least when a and b are small. A decrease in a is presumably prevented by the periodic potential mentioned above.

Calculations of the energy stored in various materials during severe work hardening have been made using Eqs. (36) and (37) together with values for the energy inside r_0. The experimental information used in these calculations is collected in Table I and the results are given in Table II. We have assumed in these calculations that a equals b. The calculations are made in two ways. First, one can determine that separation distance a which will give agreement with the experimental value of the energy stored. It is most convenient here to use as the unit of length the distance between nearest neighbors measured in the slip direction. The unit of length will thus be different for each substance considered. The results of these calculations are given in the first two rows of Table II. These results indicate that, in the most thoroughly work hardened state, dislocations are separated by about the same number of atomic spacings in different materials. A second way to make the calculation is to assume that dislocations are separated by the same number of atomic distances in different work hardened materials. The energy stored during work hardening can then be calculated and checked against the experimental value. The results of this calculation are given in the third and fourth rows of Table II. The experimental values are given in the fifth row of the table. The dislocations were assumed to be separated by 34 atomic distances in the rectangular lattice and 29 atomic distances in the diagonal lattice. These results are in remarkably good agreement with experiment except in the case of iron. The large error found for iron may be due to the fact that this metal has a different structure and a different set of slip planes. We have assumed that the axes of all line dislocations of the lattice are parallel. This is probably not the case in iron.

It might be well to point out that the results obtained with the rectangular dislocation lattice do not differ markedly from those obtained with the diagonal lattice. It is probable that neither of the lattices considered here exists in a work hardened material. We are, therefore, fortunate in finding that the results of the calculation do not depend much on the particular dislocation lattice used. The energy stored during work hardening is determined mainly by the elastic constants of the material, its density, and the value of the unit slip distance. We do not yet understand why dislocations are separated by the same number of atoms in different work hardened materials.

The separation distances of dislocations in severely work hardened materials are about 10^{-6} cm according to our calculations. For example, for copper in the case of the rectangular lattice $a=0.89\times10^{-6}$ cm; in the case of the diagonal lattice $a=0.74\times10^{-6}$ cm. This general result agrees with values for the density of dislocations in highly work hardened materials found by using other information.[11]

The author is much indebted to Professor F. Seitz for suggesting several of these problems and for many valuable discussions during the progress of the research.

[11] W. F. Brown Jr., Phys. Rev. **59**, 528 (1941); F. Seitz and T. A. Read, J. App. Phys. **12**, 178 (1941).

Letters to the Editor

Further Confirmation of the Montgomery Theory of Counter Discharge

W. E. RAMSEY AND WAYNE L. LEES
Bartol Research Foundation of the Franklin Institute, Swarthmore, Pennsylvania
July 14, 1941

THE Montgomery theory[1] of counter discharge makes it possible to predict the dependence of pulse size (maximum negative potential change of the counter wire) upon wire capacity and counter length under conditions where it is safe to assume that the discharge starts simultaneously at all points in the tube. The picture is particularly interesting if, as we vary counter length and wire capacity, the discharge passes from what has been termed a "slow" breakdown to a "fast" breakdown (for non-self-quenching gas mixtures). It follows from the discharge mechanism that for a given cylinder potential and wire capacity there is a length l_c such that for all $l \leqslant l_c$ the pulse size is constant and equal to the over-voltage on the counter. For values of $l > l_c$, $V = l\alpha/C$, where α is the charge per unit length in the positive ion sheath necessary to quench the discharge at the assigned cylinder potential. For $l < l_c$ the counter is breaking multiply in each discharge and the succession of these multiple breaks produces what has been called a slow breakdown. For $l > l_c$ the counter is "overshooting." Here there is only one break in the discharge and the counter has been referred to as having a fast breakdown.

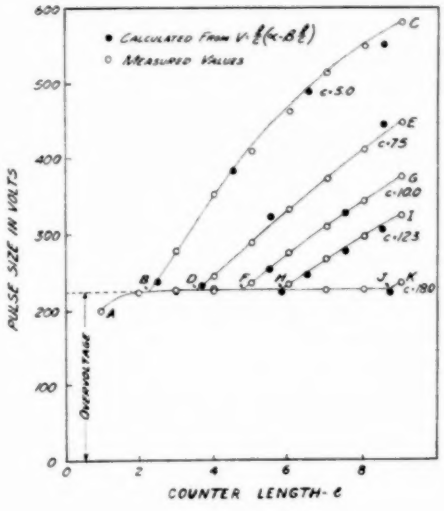

FIG. 1.

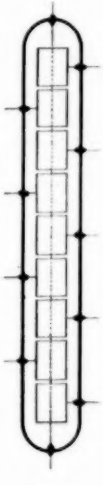

FIG. 2.

FIG. 1. Maximum potential change of counter wire and its variation with counter length for a series of wire capacities. C expressed in farads in the empirical expression, $\alpha = 5.2 \times 10^{-10}$, $\beta = 1.2 \times 10^{-22}$. Low value of A due to end effect in short counter.

FIG. 2. Counter cylinder composed of nine separately insulated segments. The number of segments above (here 225 volts above) starting potential defines the effective counter length, other segments being at a value below the starting potential. Thus by changing the potential of the segments the effective counter length may be changed *without altering capacity of the wire system.* Capacity changes were made by adding condensers between wire and ground. Voltage swing measured using a weakly coupled electrometer tube and grounding counter wire with key after each discharge. Counter filled with 9 cm argon-oxygen mixture.

If the discharge does not start at all points in the tube within a short time interval (10^{-7} second) after it has started at one point, the linear charge density will not be constant over the counter length and the picture, although unaltered in form, is modified somewhat in detail to allow for the finite time required for the discharge to propagate itself from one point to another. Simple considerations combined with direct observations on the time variation of counter wire potential[2] indicate that this time of propagation is only important in modifying the picture for small C and large l.

Figure 1 is a family of curves showing the variation of pulse size with l for a series of values of C. Here great care was taken in the experimental procedure to obtain low values of C, *variation of l without altering C*, and a true value of the maximum negative voltage when no charge is allowed to leak from the counter wire. Refer to Fig. 2 and its caption for a description of the procedure.

In Fig. 1, ABC is the characteristic for $C = 5.0\mu\mu f$, ADE for the wire capacity C equal to $7.5\mu\mu f$, AFG for $C = 10.0\mu\mu f$, and so on. Examination of this family reveals that the lengths AB, AD, AF, AH, AJ (values of l_c) are proportional to C. The family may be represented satisfactorily by the relation $V = \text{Constant} = \text{over-voltage}$ for values of $l \leqslant l_c$ and $V = (l/C)[\alpha - \beta(l/C)]$ for values of $l \geqslant l_c$. Here α is the constant charge per unit length referred to above and experimentally obtained for small l and large C. Thus to a first approximation propagation time reduces the average charge per unit length by an amount proportional to l/C.

The experimental picture obtained agrees with the picture presented by the theory, altered only to allow for propagation times of the order of 10^{-7} second. The authors have been unable to reconcile the results obtained with any picture of the discharge differing materially from that presented by this theory.

[1] C. G. Montgomery and D. D. Montgomery, Phys. Rev. **57**, 1030 (1940).
[2] W. E. Ramsey, Phys. Rev. **57**, 1022 (1940).

New Reactions in Nickel

R. L. DORAN, *Purdue University, Lafayette, Indiana*
AND
W. J. HENDERSON, *National Research Council, Ottawa, Ontario, Canada*
August 7, 1941

KONOPINSKI has shown[1] that the half-lives of many radioactive nuclei show certain regularities when expressed as functions of their atomic numbers. These regularities occur in families of nuclei that differ only in the number of alpha-particle units that they contain. If the logarithm of the period is plotted against the atomic number for a given family, the resulting curves may be interpolated to make predictions about unknown and uncertain members of the family.

Curves of the families containing radioactive isotopes of nickel are drawn in Fig. 1. According to the predictions of these curves, Ni^{57} should have a half-life of about 2 minutes and Ni^{59} a half-life of about 36 hours. A period of 36 hours

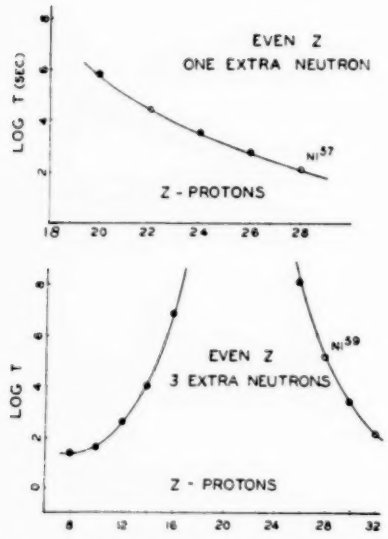

FIG. 1. Log of half-life T as a function of atomic number Z.

is known in nickel but it has been assigned[2] to Ni^{57} since such an activity was not observed with slow neutron or deuteron bombardment of nickel.

In the present work the 36-hour activity was produced by a fast neutron reaction on nickel. In addition, two other periods of 2 minutes and 2.6 hours were observed. The 2.6-hour activity has been definitely assigned[3] to Ni^{63}. Also, alpha-particle bombardments of iron showed the 2-minute and the 36-hour activities. The activities are then to be assigned to Ni^{57} and Ni^{59}, since the stable isotopes of iron which could produce radioactive nickel by the (alpha, n) process are Fe^{54} and Fe^{56}. Long bombardments of nickel by slow neutrons produced a weak 36-hour activity which was followed over 4 half-lives. This period was also produced by deuteron bombardments of nickel. In both cases the activity was a positron activity of 36 hours half-life, and must be due to the formation of Ni^{59} by Ni^{58} (n, gamma) and Ni^{58} (d, p) reactions.

The establishment of Ni^{59} to have a half-life of 36 ± 1 hours leads to the assignment of the 2 minutes and was produced by a Fe^{54} (alpha, n) and a Ni^{58} (n, $2n$) reaction. Chemical separations for nickel were made throughout.

[1] Konopinski and Dickson, Phys. Rev. **58**, 949 (1940).
[2] Livingood and Seaborg, Phys. Rev. **53**, 765 (1938).
[3] Heyn, Physica **4**, 1224 (1937).

The Antisymmetrical Interaction in Beta-Decay Theory

CHARLES L. CRITCHFIELD* AND EUGENE P. WIGNER
Princeton University, Princeton, New Jersey
August 2, 1941

THE process of beta-disintegration can be considered as a four-particle process, i.e., a process in which four particles are created simultaneously. Thus, e.g., the process leading to the emission of an electron can be considered as the creation of a proton, a neutrino, and an electron in positive energy states, and of a neutron in a negative state.

If one adopts this point of view, it appears natural to look for interactions which are either totally symmetric or totally antisymmetric in the four particles. We found that a relativistically invariant interaction which does not contain any derivatives of wave functions[1] cannot be symmetric in the particles. There is, however, a totally antisymmetric relativistically invariant interaction which can be used instead of the "vector interaction" originally proposed.[1]

In terms of the customary five invariants (heavy particle covariants contracted on light particle contravariants) the antisymmetric interaction is a sum of scalar, axial vector and pseudoscalar invariants. An axial vector interaction has already been introduced by Gamow and Teller[2] as an alternative to the polar vector in order to allow beta-transitions in which $\Delta i=\pm1$ and 0 (but no $0\rightarrow0$). The antisymmetric interaction thus permits $\Delta i=0$, ±1, *including* $0\rightarrow0$ and with stronger transitions with $\Delta i=0$ than in the pure axial vector interaction. There is no change of parity in the allowed transitions.

Certain qualitative aspects of allowed transitions under the antisymmetric interaction can be seen at once. There is an additional cause for the transitions $\Delta i=0$. In consequence thereof, the theory gives a larger ratio for the lifetimes of the light $4n+2$ nuclei to the lifetimes of the light odd nuclei than the Gamow-Teller theory gave.[3] This increases the discrepancy in the case of He^6 but decreases it in most other cases. However, the theory does not help in understanding the great irregularity in the lifetimes of the $4n+2$ nuclei. On the other hand, the theoretical ratio of the number of transitions to excited and ground states of the odd nuclei studied by Grönblom[4] is improved in every case.

Forbidden transitions in this theory are qualitatively the same as under the axial vector interaction. First forbidden spectra are of two types: one identical with allowed spectra in shape and due to the finite velocity of the nuclear particles; the other distinctly different in shape and arising from the finite radius of the nucleus. The change of nuclear spin is always zero for the first type (including $0\rightarrow0$) but in the second type the spin may change by ±1 or ±2. All the first forbidden transitions incur a change in parity.

The nature of the departure of forbidden spectra from the form of the allowed spectra can be determined as follows. An electron with the full amount of energy available in a given process has a shorter wave-length than a neutrino with the full amount available to it because of the finite rest energy of the electron. Thus the forbidden spectrum of any degree, if proportional to a power of $r_{\text{nuc}}/\lambda_{\text{light part}}$, will tend to be more intense at high electron energies than at low. The obvious effect on the Kurie plot is to make it concave toward the axes at high electron energies. None of the carefully measured spectra are of this character, and, in fact, in most cases the tendency is to the opposite curvature.

Careful measurements on the spectra of Na^{24} and P^{32} by Lawson[5] yield Kurie plots which are good straight lines at the high energy end. According to the present theory it would appear that these transitions are either allowed or

first forbidden of the first type; but this indication is not quite peculiar to our theory. The above argument concerning the spectrum suggests that the same conclusion would be reached in any choice of invariants except, perhaps, in certain special cases. This general result may be interpreted to mean that the long-lived elements are not long-lived for the most part because of forbidden spin or parity change, or it may mean that the application of beta-decay theory must be further refined.

Second forbidden transitions in this theory show no change of parity and $\Delta i = \pm 2, \pm 3$. The shape of these Kurie plots is concave to the axis at high energy for all matrix elements.

We are indebted to Professors Konopinski and Uhlenbeck for helpful discussions of this subject at the Washington Conference and to the former for access to his review article on beta-decay before publication.

* National Research Fellow.
[1] E. Fermi, Zeits. f. Physik **88**, 161 (1934).
[2] G. Gamow and E. Teller, Phys. Rev. **49**, 895 (1936).
[3] E. Wigner, Phys. Rev. **56**, 526 (1939).
[4] B. Grönblom, Phys. Rev. **56**, 508 (1939).
[5] J. Lawson, Phys. Rev. **56**, 131 (1939).

The Second Maximum of the Rossi Curve

LEO BROUSSARD AND ALVIN C. GRAVES
Department of Physics, The University of Texas, Austin, Texas
August 11, 1941

SINCE Schmeiser and Bothe[1] reported that the second maximum in the Rossi transition curve at about 17 cm of lead is due to small angle showers a number of investigations have been made on this maximum. The results have been somewhat contradictory as to the height of the maximum and angular divergence of showers responsible for the maximum. In view of this contradiction in data taken mainly with counters, it was thought worth while to investigate this problem with a cloud chamber. This method would eliminate the uncertainty in angle inherent in counter measurements as well as the masking effect of counter background.

The apparatus used consisted of a vertical, counter-controlled, cloud chamber and a vacuum tube time delay control circuit. By means of a mirror system a camera took two pictures 54° apart. All lead was placed above the top counter so that non-ionizing particles as well as ionizing particles might cause an expansion.

The results obtained are shown in Fig. 1. More than 200 showers were recorded for each point near the maximum so that the probable error for these points is less than 5 percent. The Rossi curve for the total showers recorded has a definite maximum at about 17 cm of lead. The rise in the curve (nearly 30 percent) is well above the probable error as computed from the number of showers. The second curve is for two-particle showers with angular divergence greater than 20°. The similarity of the two curves suggests that the maximum is mainly due to this component. So few narrow angle showers were obtained that it was impossible to construct a similar curve for them or to draw any conclusions as to whether or not they exhibit a different behavior in the neighborhood of the maximum. A curve of

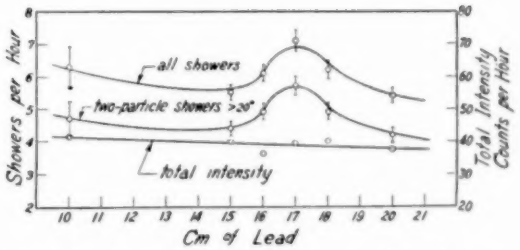

FIG. 1. Total intensity and shower intensity of cosmic rays.

total intensity on a different scale is included for purposes of comparison. It was obtained from the photographs used in obtaining the shower curves.

[1] K. Schmeiser and W. Bothe, Naturwiss. **25**, 669 (1937).

Production of Mesotrons by Ionizing Radiation

WILSON M. POWELL*
Kenyon College Cosmic-Ray Trailer Laboratory, Summit of Mount Evans, Idaho Springs, Colorado
August 4, 1941

IN a series of 3881 random expansions of a large Wilson cloud chamber containing five horizontal lead plates each 1 cm thick one photograph was obtained which can be interpreted as the production by a heavy particle of a shower containing at least four heavy particles and possibly more. (Fig. 1).

The incoming particle must pass through a half-inch of cold rolled steel to enter the chamber. If it were an electron it is extremely unlikely that it would be unaccompanied by shower particles. The energy of the incoming particle must be quite great to produce such a shower, and this would almost insure the presence of shower particles if it were an electron.

The short heavy track appearing directly under the top plate is either a mesotron or a proton. The track which

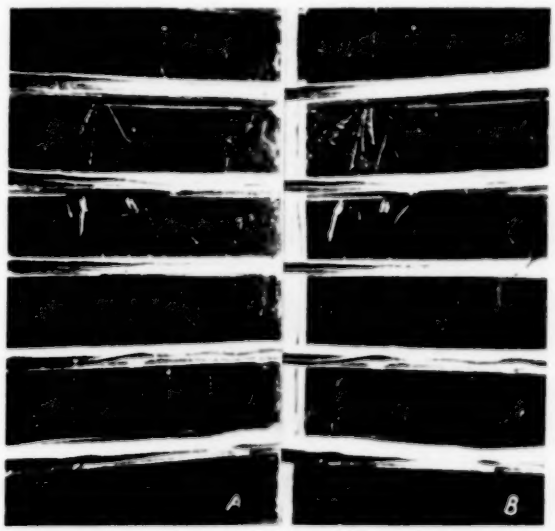

FIG. 1. Wilson cloud-chamber photograph. Each lead plate is 1 cm thick. Figures *A* and *B* were taken at 30° to the left and right of normal.

penetrates the second lead plate and then becomes very thick and passes out of the front of the chamber may be a proton. The upper part of the track appears slightly brighter than the neighboring rays. This would indicate that the particle was a proton. On the other hand the ray is coming towards the cameras and is the only one which is in the very front of the chamber, and the brightness of the upper part of the track may be due to these two conditions. If this is true the particle is a mesotron. The great increase in ionization in passing through the plate is a little larger than that usually observed for a proton.

A ray on the left-hand side passes through two plates without producing secondaries and then disappears in the back of the chamber. This particle is either a mesotron or a proton. A ray to the right passes through three lead plates without producing secondaries and is either a mesotron or a proton. It passes out of the back of the chamber. The ray bounding the right-hand edge of the shower passes through one lead plate without producing secondaries and passes out of the back of the chamber. This might be an electron but is more likely to be a heavy particle.

The shower might be interpreted as a nuclear disintegration where all the fragments were protons of high energy. On the other hand most disintegrations of this type send particles equally in all directions. The most likely interpretation seems to be that the incoming particle is a proton of high energy and the shower consists of mesotrons.

This work is supported by the Rumford Fund for the Study of Radiation of the American Academy of Arts and Sciences, the Penrose Fund of the American Philosophical Society, the Fund for Astrophysical Research, and the John Simon Guggenheim Memorial Foundation.

* Guggenheim Fellow.

Cloud-Chamber Photograph of Slow Mesotron Pair

DONALD J. HUGHES*
University of Sao Paulo, Sao Paulo, Brazil
August 10, 1941

DURING July, some 5000 photographs have been taken with a cloud chamber in a field of 1165 gauss at an altitude of 15,500 feet at San Cristobal mine, Peru. As a complete discussion of the results obtained may not appear for some time, it seems desirable to report now on one picture of some interest. The numerical results given here are those reported at the cosmic-ray symposium in Rio de Janeiro, August 3–9, and are admittedly rough, there having been no opportunity as yet for precise measurement of the film.

Figure 1 shows several shower electrons. a contamination α-particle and a positive-negative pair of heavily ionizing particles. Stereoscopic examination shows the pair to be in the same plane, which is not the plane of the other tracks, and proceeding from a point in or near the front glass plate of the chamber.

The right-hand particle (negative) has an $H\rho$ value of 1.03×10^5 gauss cm. Its ionization (estimated from the original negative) is about 4 to 6 times the electronic minimum. Corresponding to this variation, the calculated

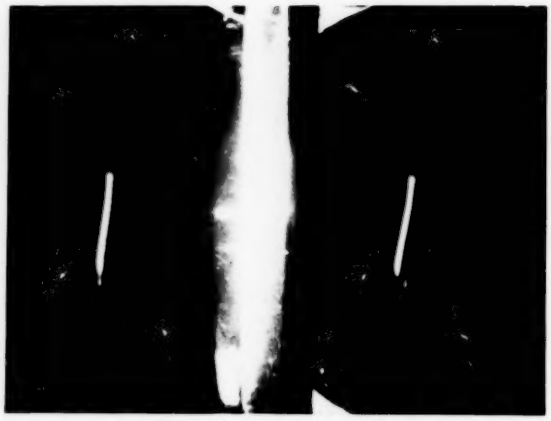

FIG. 1. Slow mesotron pair.

mesotron mass will range from 160 to 196 electron masses. The ionization density can also be estimated from the fact that it is very nearly equal to that of the knock-on electron. The known range of the latter (hence its velocity) gives an ionization value of 4.5. A value equal to this for the mesotron results in a mass of 170. The particle cannot be a proton, for with the $H\rho$ value observed it would have a range of only 1.2 cm in the chamber.

The energy and angle of ejection of the knock-on furnishes an additional independent mass determination. As it ends in the chamber its range, and hence its energy, can be easily obtained, the latter being 34 kev. The angle of ejection is estimated as lying in the range 50°–60°, which gives a mesotron mass of 189 ± 24. If the incident particle were electronic, the knock-on energy would be 320 kev at 60° and even more for smaller angles—an impossible value.

The mass of the left-hand (positive) particle cannot be fixed as accurately as the other for there is no knock-on and the curvature is not as constant. For the present it must suffice to say that the ionization and $H\rho$ values are very close to those of the negative particle and the mass is of the same order of magnitude—about 180 electron masses.

Though later calculations will probably change to some extent the quantitative results, it seems reasonable to conclude that we have here observed the creation of a pair of slow mesotrons ($KE\approx5$ Mev) either in the gas or glass wall of the cloud chamber. The production of mesotrons at this altitude has also been shown by the occurrence of related penetrating, non-multiplying rays in cloud chambers. Dr. Wollan has observed several such cases during the present experiments. The results with the magnetic field, however, furnish in addition information on the mass and energy of the particles. About sixteen heavy tracks with measurable curvature have been obtained and will be reported on later.

We wish to thank the Cerro de Pasco Corporation for their hospitality and the use of many facilities during these observations. The Academy of Science of Brazil and the faculty of Sao Paulo University have rendered great assistance to us during our stay in Brazil for which we are deeply grateful.

* University of Chicago, Chicago, Illinois.